

A Precision Measurement of the η Radiative Decay Width via the Primakoff Effect

Dec 14, 2009

A. Gasparian (spokesperson), P. Ambrozewicz, R. Pedroni
North Carolina A&T State University, Greensboro, NC

L. Gan (co-spokesperson), T. Black
University of North Carolina Wilmington, Wilmington, NC

D. Dale
Idaho State University, Pocatello, ID

D. Lawrence, Elton Smith, A. Somov
Thomas Jefferson National Accelerator Facility, Newport News, VA

M. Khandaker, V. Punjabi, C. Salgado
Norfolk State University, Norfolk, VA

A. Dolgolenko, M. Kubantsev, I. Larin
Institute for Theoretical and Experimental Physics, Moscow, Russia

A. Ponosov, D. Romanov, V. Tarasov
Moscow Engineering Physics Institute, Moscow, Russia

J. Goity
Hampton University, Hampton, VA

S. Gevorkyan
Joint Institute for Nuclear Research, Dubna, Russia

D. McNulty
University of Massachusetts, Amherst, MA

G. Lolos, A. Semenov, Z. Papandreous
University of Regina, Regina, Saskatchewan, Canada

V. Crede, N. Sparks
Florida State University, Tallahassee, FL

T.E. Rodrigues
University of São Paulo, São Paulo, Brazil

X. Yan, Y. Ye, P. Zhu
University of Sci. & Tech. of China, Hefei, China

H. Lu
University of HuangShan, Hefei, China

Contents

1	Introduction	5
2	Motivation	5
3	Previous Measurements of the η Radiative Width	10
4	Measurement of the η Radiative Width via the Primakoff Effect	11
5	Choice of Primakoff Targets	15
6	Experimental Setup	17
6.1	High Energy Photon Tagger	18
6.2	Pair Spectrometer	20
6.3	Targets	22
6.4	Forward Electromagnetic Calorimeter (FCAL)	23
6.5	Compton Calorimeter (CompCal)	24
7	Acceptance, Resolutions and Event Selection	25
7.1	Geometrical Acceptance	25
7.2	Experimental Resolutions	26
7.3	Event Selection	28
8	Background Simulation	29
8.1	Accidental Background	32
8.2	Combinatorial Background	33
8.3	Reactions with an η in the Final State	33
8.4	Sensitivity of $\Gamma_{\eta \rightarrow \gamma\gamma}$ Determination to Backgrounds	37
9	Rates, Uncertainties, and Beam Time Request	40
9.1	Production Rates	40
9.2	Uncertainties	42
9.3	Beam Time Request	43
10	Verification of the Systematic Error with Compton Scattering	44
11	Trigger and Data Acquisition	48
12	Contribution to the Hall D Base Instrumentation	48
13	Summary	50

Abstract

We propose to perform a measurement of the $\eta \rightarrow \gamma\gamma$ decay width at a 3% precision via the Primakoff effect in Hall D with the GlueX standard setup. This experiment will not only resolve a long standing puzzle of the experimental discrepancy between the Primakoff and collider measurement results, but will also significantly reduce the overall error bar on this important quantity, resulting in a direct improvement on all other partial η decay widths. A high precision measurement of the $\eta \rightarrow \gamma\gamma$ decay width will have significant impact on the experimental determination of fundamental parameters, such as the ratios of the light quark masses (m_u, m_d, m_s) and the $\eta - \eta'$ mixing angle, and will provide a sensitive test of QCD symmetries in the chiral limit. This experiment will also deliver the first cross section measurement on the $\gamma p \rightarrow \eta p$ elementary process at the forward angles in the 10 GeV energy range.

1 Introduction

The availability of high quality, high duty factor 12 GeV electron beams at Jefferson Lab will enable unprecedented new opportunities to perform precise measurements of the electromagnetic properties of pseudoscalar mesons. We have developed a comprehensive experimental program in the last ten years to study the two photon decay widths, $\Gamma_{\gamma\gamma}$, and the transition form factors, $F_{\gamma\gamma^*}$, of the π^0 , η , and η' pseudoscalar mesons. The original proposal was presented to the JLab PAC18 special review in July 2000. It received a high recommendation from the PAC [1] and was identified in the “Executive Summary” of the CEBAF 12 GeV upgrade white paper “Science Driving the 12 GeV CEBAF Upgrade” as one of the major physics programs for the lab’s long-range plan. This project was re-confirmed by PAC23 in 2003 and PAC27 in 2005 (the 12 GeV special reviews). It remains a top priority physics program with the PAC recommendation “to be developed as one of the leading scientific projects for the next generation of experiments at Jefferson Lab” [2]. The measurement of the η radiative decay width described below will be the first experiment among a series of other measurements in the Primakoff 12 GeV program.

2 Motivation

The η meson is of great importance for the understanding of fundamental aspects of QCD. In the chiral limit, the condensation of quark-anti-quark pairs in the QCD vacuum spontaneously breaks $SU_L(3) \times SU_R(3)$ symmetry down to the flavor $SU(3)$ symmetry. As a result, there are eight massless Goldstone Bosons corresponding to the eight spontaneously broken symmetry generators. These Goldstone Bosons are identified with the octet of pseudoscalar mesons (π^0 , π^\pm , K^\pm , K^0 , \bar{K}^0 , and η). In reality, the quark masses are non zero (albeit small), thus breaking the chiral symmetry explicitly and giving rise to masses for the Goldstone Bosons following the mechanism discovered by Gell-Mann, Oakes and Renner [3]. As the heaviest member in the octet pseudoscalar meson family, the η plays a special role. It has an interesting feature that all its strong and electromagnetic decays are forbidden in lowest order due to P, PC, C, G-parity symmetries and angular momentum conservation [4]. The width of the η is about five orders of magnitude smaller than a typical strong decay, such as the ρ and ω mesons. This feature makes η decay 10^5 times more sensitive than the ρ and ω decays at a comparable branching ratio for testing symmetries of QCD.

The two-photon decay of the η is directly associated with the chiral anomaly. This is one of the most profound symmetry aspects in QCD, namely, the explicit breaking of a classical symmetry by the quantum fluctuations of the quark fields when they couple to a gauge field. This phenomenon is of a pure quantum mechanical origin and can be calculated exactly at all orders in the chiral limit. In QCD there are several observable phenomena that originate from anomalies. One connected to the couplings of the quarks to the gluons is responsible for the non-zero mass of the η' at the chiral limit. The axial anomaly related to the η two-photon decay involves the corresponding coupling of the quarks to photons [5]. In the chiral and large N_c limits, the two-photon decay of the η can be predicted. Important questions are related to the effects of the quarks masses and the corrections due to the fact

that $N_c = 3$.

Indeed, the relatively straightforward situation of the chiral limit becomes more complex in the case in which the quark masses are non-vanishing. In the real world the current quark masses are estimated to be $m_u \sim m_d/2 \sim 5$ MeV and $m_s \sim 150$ MeV at the renormalization QCD scale of about 1 GeV. These masses make the η massive, while $SU(3)$ and isospin breaking by the unequal quark masses induce mixings among the π^0 , η and η' mesons. The $SU(3)$ breaking is primarily manifested by η mixing with the $U_A(1)$ quasi-Goldstone Boson, the η' , and the isospin breaking by the mass difference $m_d - m_u$ is responsible for the G-parity violating decays $\eta \rightarrow 3\pi^0$ and $\eta \rightarrow \pi^+\pi^-\pi^0$. It should also be mentioned that the η and η' mixings with the π^0 , driven by $m_d - m_u$ predict an increase in the width of $\pi^0 \rightarrow \gamma\gamma$ of about 4% [6, 7].

Theoretically, the decays $\eta \rightarrow \gamma\gamma$ and $\eta' \rightarrow \gamma\gamma$ must be analyzed together. This is because $SU(3)$ symmetry breaking by m_s induces an important mixing effect between the pure $SU(3)$ states, namely the octet η denoted by η_8 and the singlet η denoted by η_0 . The physical η and η' states are given by:

$$\begin{pmatrix} \eta \\ \eta' \end{pmatrix} = M(\theta) \begin{pmatrix} \eta_8 \\ \eta_0 \end{pmatrix} = \begin{pmatrix} \cos \theta & -\sin \theta \\ \sin \theta & \cos \theta \end{pmatrix} \begin{pmatrix} \eta_8 \\ \eta_0 \end{pmatrix}, \quad (1)$$

where θ is the mixing angle. The decay amplitudes into two photons of the pure $SU(3)$ states are determined by the chiral anomalies of the corresponding axial currents and by the meson decay constants. The decay amplitudes of the physical states involve key effects due to the state mixing just mentioned and corrections to decay constants due to the quark masses. The latter corrections lead to a decay constant matrix [8, 9]:

$$F = \begin{pmatrix} F_{88} & F_{80} \\ F_{80} & F_{00} \end{pmatrix} \quad (2)$$

The theoretical approach to the analysis of these effects is based on Chiral Perturbation Theory (ChPT) along with an expansion in $1/N_c$ where $N_c = 3$ is the number of colors in QCD [6, 7, 8, 10]. The decay constant F_{88} and F_{80} can be determined from our knowledge of F_π , F_K and the pseudoscalar masses. Thus, state mixing and decay constants involve two unknowns, namely the mixing angle θ and the next to leading order correction to F_{00} . In addition, at next to leading chiral order there is a new low energy constant (LEC) which has to be taken into account for the decay into two photons. That LEC has been estimated using QCD sum rules [7] ($t_1 \sim -F_\pi^2/m_\rho^4$), an estimate that one would expect to be correct within the typical 30% accuracy of these sum rules. With this estimate, one can use the measured widths $\Gamma_{\eta \rightarrow \gamma\gamma}$ and $\Gamma_{\eta' \rightarrow \gamma\gamma}$ to determine the mixing angle and the NLO correction to F_{00} [6]. The $\eta - \pi^0$ mixing has a small effect on the η decay, leading to a reduction of $\Gamma_{\eta \rightarrow \gamma\gamma}$ by less than 1.5%, which is below the level of resolution of the proposed measurement.

The decay widths at next to leading order in the chiral and $1/N_c$ expansions are given by [6]:

$$\Gamma_{\eta^{(\prime)} \rightarrow \gamma\gamma} = \frac{M_{\eta^{(\prime)}}^3}{4\pi} |\kappa_{\eta^{(\prime)}}|^2 \quad (3)$$

where [6]

$$\begin{pmatrix} \kappa_\eta \\ \kappa_{\eta'} \end{pmatrix} = -i\alpha \left(\frac{1}{4\pi} \frac{1}{\sqrt{3}} ((M(\theta)F)^{-1})^T \begin{pmatrix} 1 \\ \sqrt{8} \end{pmatrix} + \pi \frac{t_1}{9\sqrt{3}F_\pi} M(\theta) \begin{pmatrix} 7M_\pi^2 - 4M_K^2 \\ \sqrt{8}(2M_\pi^2 + M_K^2) \end{pmatrix} \right) \quad (4)$$

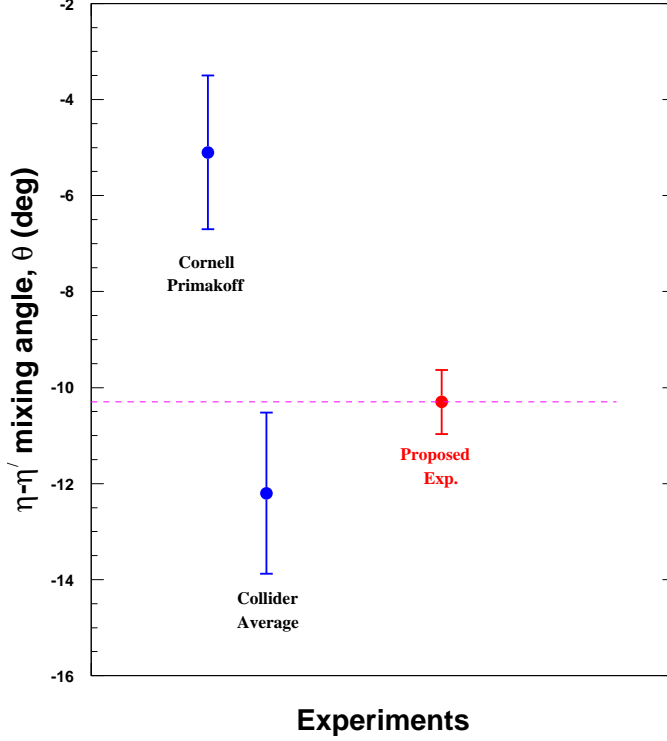


Figure 1: The importance of $\Gamma_{\eta \rightarrow \gamma\gamma}$ in the determination of $\eta - \eta'$ mixing angle. The first two points are mixing angles calculated using existing $\Gamma_{\eta \rightarrow \gamma\gamma}$ data from the Primakoff [22] and average of e^+e^- [17] results. Point 3 is the expected error calculated by using the proposed experimental result, arbitrarily plotted to agree with the value calculated using the average Primakoff [22] and e^+e^- [17] results. The plotted uncertainties combine the experimental and theoretical errors in quadrature.

The mixing angle θ is determined through formulas (3) and (4), where the latter was obtained to next-to-leading order in the chiral expansion. Using the best fit to the current widths as provided by the Particle Data Group (average of Primakoff and the e^+e^- collision experimental results) one obtains [6] $\theta = -10.6 \pm 2.0$ deg. The error in $\Gamma_{\eta \rightarrow \gamma\gamma}$ gives an uncertainty in θ which can be estimated by $\delta\theta \sim -\frac{\delta\Gamma_{\eta \rightarrow \gamma\gamma}}{\Gamma_{\eta \rightarrow \gamma\gamma}} \times 15$ deg. Thus a 3% accuracy in the measurement of the η width would yield a 0.45° uncertainty in the mixing angle. The uncertainty in the $\Gamma_{\eta' \rightarrow \gamma\gamma}$ width has less impact on the angle, as it mostly affects the value of

F_{00} in the decay constant matrix. There is additional theoretical uncertainty in the mixing angle which has to do with the corrections of next-to-next-to-leading order in the chiral expansion of formula (4), and which is difficult to quantify at this point. Figure 1 shows the mixing angle determined using previous Primakoff [22] and e^+e^- [17] experimental results on $\Gamma_{\eta \rightarrow \gamma\gamma}$. As one can see, the proposed new measurement on $\Gamma_{\eta \rightarrow \gamma\gamma}$ with 3% precision will significantly improve the uncertainty in the mixing angle. The most important impact of an accurate measurement of $\Gamma_{\eta \rightarrow \gamma\gamma}$ will be in solving the discrepancy between the Primakoff and the e^+e^- experimental results for the η decay width. In particular, this current discrepancy translates into a difference of more than 6° for the mixing angle obtained in the two types of measurements.

The fact that there is a well defined theoretical framework makes the η a very important state to be studied with precision as a mean to further understand fundamental aspects of QCD. While the width of the $\pi^0 \rightarrow \gamma\gamma$ will provide the most precise test of the chiral anomaly prediction at leading order, the $\eta \rightarrow \gamma\gamma$ decay will be the most sensitive probe for the higher order corrections due to its larger mass. In particular, a precise measurement of $\Gamma_{\eta \rightarrow \gamma\gamma}$ is crucial to extract the η and η' mixing angle and their decay constants as discussed above.

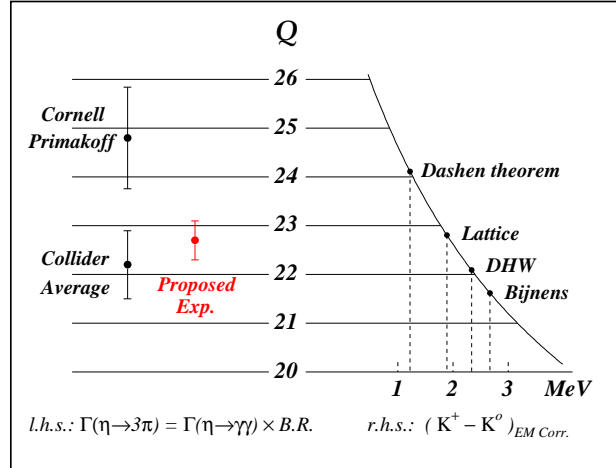


Figure 2: The importance of $\Gamma_{\eta \rightarrow \gamma\gamma}$ in the measurement of quark mass ratio Q . The *l.h.s.* indicates the values of Q corresponding to the Primakoff and collider experimental results for the $\Gamma_{\eta \rightarrow \gamma\gamma}$. The *r.h.s.* shows the results for Q obtained with four different theoretical estimates for the electromagnetic self energies of the kaons. Taken from Ref. [12].

One important question to ask is: What would be the broad impact of a more precise measurement of the η two-photon partial width? Right away, it would imply a corresponding improvement in the determination of all other partial widths of the η , as these are determined

using the two-photon widths and the corresponding branching ratios. This would therefore have wide range implications. One decay that is particularly important is the $\eta \rightarrow \pi\pi\pi$ decay (two different final states). The decays of $\eta \rightarrow \pi^+\pi^-\pi^0$ and $\eta \rightarrow \pi^0\pi^0\pi^0$ can only proceed through the isospin symmetry breaking by the quark mass difference $m_d - m_u$, and thus provide a sensitive way to determine the quark mass ratio $(m_u - m_d)/m_s$. The analysis of extraction of quark mass ratio from the isospin breaking observables was carried out by Leutwyler [12]. In his analysis, a quark mass ratio is defined as

$$Q^2 = \frac{m_s^2 - \hat{m}^2}{m_d^2 - m_u^2}, \quad (5)$$

where $\hat{m} = (m_u + m_d)/2$.

There are two ways to determine the Q value. One way is by means of a ratio of meson masses:

$$Q^2 = \frac{M_K^2}{M_\pi^2} \frac{M_K^2 - M_\pi^2}{(M_{K^0}^2 - M_{K^+}^2)_{QCD}} [1 + O(m_{quark}^2)] \quad (6)$$

The major problem in extracting Q from this relation arises from the theoretical uncertainties in the determination of the electromagnetic contributions to the $K^0 - K^+$ mass difference, because the only piece of $K^0 - K^+$ mass difference in the denominator of formula 6 is due to the $m_d - m_u$. As shown in the right hand side of Figure 2, the Q values determined by this approach have strong model dependence. One may expect that lattice QCD will provide more accurate calculations to determine the electromagnetic corrections in the future; however, it is not clear at the moment when this would happen.

Another way to extract Q is by means of $\eta \rightarrow \pi\pi\pi$ decays that have negligibly small electromagnetic corrections due to chiral symmetry, in particular for the $\eta \rightarrow \pi^0\pi^0\pi^0$ decay channel. The $\eta \rightarrow \pi\pi\pi$ decay width is related to the Q value through a relation $\Gamma_{\eta \rightarrow \pi^+\pi^-\pi^0} \propto 1/Q^4$. This second approach thus represents a more sensitive probe of the symmetry breaking generated by $m_d - m_u$, and has the potential to deliver accurate quark mass ratios [14]. As emphasized by Leutwyler [12], the main errors in determining Q using $\eta \rightarrow \pi\pi\pi$ decays are due to the experimental uncertainties in the partial width $\Gamma_{\eta \rightarrow \pi\pi\pi}$ that are determined by the two-photon widths $\Gamma_{\eta \rightarrow \gamma\gamma}$ and the well known branching ratios ($(32.56 \pm 0.23)\%$ for $\eta \rightarrow 3\pi^0$ and $(22.73 \pm 0.28)\%$ for $\eta \rightarrow \pi^+\pi^0\pi^-$ [13]). The two different methods of measuring $\Gamma_{\eta \rightarrow \gamma\gamma}$ (photon-photon collisions and the Primakoff effect) yield conflicting results, as shown in the left hand side of Figure 2. This is an important example of the impact that the precise measurement of the η two-photon widths would have for determining fundamental parameters of QCD. In addition, there have been intensive theoretical activities in recent years to improve the accuracy of extracting the quark mass ratio through the η decays. The calculations of the decays within chiral perturbation theory supplemented with dispersion relations have been carried out in reference [15], and currently new theoretical efforts to improve that calculation are underway [16], where the most recent measurements at KLOE [18], MAMI [19] and WASA [20] are used in order to improve the accuracy of the inputs to the dispersion relations. The two-loop chiral perturbation theory calculation needed to determine the subtractions involved in the mentioned dispersion analyses has already been

carried out [21]. The availability of new high precision experimental results will certainly utilize these new results and inspire further theoretical efforts in chiral perturbation theory.

In summary, due to its relatively larger mass, the η meson represents a sensitive probe for studying QCD symmetries and symmetry breaking at low energy. The spontaneous chiral symmetry breaking gives birth to the η as a Goldstone particle and the chiral axial anomaly primarily determines the $\eta \rightarrow \gamma\gamma$ decay width. It is sensitive to both $SU(3)$ symmetry breaking by the strange quark mass and to isospin symmetry breaking by the mass difference $m_d - m_u$. The symmetry breaking manifests itself in state mixing effects which have an important impact in the decays of the η meson. It opens a window on the determination of fundamental aspects of QCD in a model-independent manner, such as the light quark-mass ratio $((m_d - m_u)/m_s)$, the η - η' mixing angle and the decay constants. In addition, precision measurement of radiative η decay width will improve all other η partial decay widths. As a result, precision measurements of the $\eta \rightarrow \gamma\gamma$ decay width will have a wide ranging impact on understanding QCD at the confinement scale. It will also further stimulate theoretical improvements, in particular in the framework of chiral perturbation theory. In addition, this experiment will also deliver the first cross section measurement on the $\gamma p \rightarrow \eta p$ elementary process in 10 GeV energy range at the forward angles, which will provide important inputs in the extraction of the η photoproduction amplitude on the nucleon.

3 Previous Measurements of the η Radiative Width

The present experimental knowledge of the η meson width is presented in figure 3 [17], along with the projected measurement which could be made with 12 GeV at Jefferson Lab. Most of the measurements in the figure have been performed using two photon interactions in e^+e^- collisions. One exception is the Cornell measurement of the η width [22] via the Primakoff effect. This gives a reported width which is significantly lower (at the 3σ level) than those from e^+e^- collisions. The Particle Data Group had listed both two-photon and Primakoff measurements for more than 30 years because there was “no compelling reason” [23] to exclude the Cornell Primakoff result. After more than 30 years without new Primakoff experimental confirmation, the Cornell result was removed from the Particle Data Group in 2006 following the advice of Nefkens[4]. On the other hand, using the same apparatus, the Cornell group measured the $\Gamma_{\pi^0 \rightarrow \gamma\gamma} = 7.93 \pm 0.39$ eV [24] in good agreement with the world average value of 7.74 ± 0.55 eV. From the experimental point of view, the major differences between the Cornell group’s π^0 result and their η result are: (1), the resolutions of reconstructed meson invariant mass and production angle for the π^0 case were made better than the η case by doubling the distance between the target and the photon detector (calorimeter), which helps to give a better background subtraction and to discern the characteristic shapes of the different production mechanisms; (2), their π^0 data covered larger production angles than the η by taking special runs at the larger angles where the nuclear coherent production dominates, which helps in extracting the nuclear coherent amplitude; (3), there is less overlap between the Primakoff production and the nuclear background in the π^0 measurement than in the η due to the smaller mass of the pion; and (4), the Primakoff

π^0 production is peaked at smaller q^2 than the η , making the fit less sensitive to details of charge form factor calculations.

Since the days of Cornell's Primakoff measurements in 1974, both experimental techniques and theoretical calculations required for Primakoff experiments have been improved greatly. On the experimental side, a high energy and high precision tagged photon beam has become available. The high beam intensity opens a possibility to choose light targets, such as hydrogen target. Novel calorimetry based on new fast crystals (such as PbWO_4) have been developed with high position and energy resolutions. On the theoretical side, the light pseudoscalar meson photoproduction amplitudes in the electromagnetic and strong fields of nuclei at forward direction have been extensively studied by theoretical calculations based on the Glauber theory of multiple scattering [25]. In particular, the effects of final state interactions, corrections for light nuclei, contributions from nuclear collective excitations, and photon shadowing in nuclei have been considered. Nuclear incoherent η photoproduction has also been extensively investigated using both Glauber theory [26] and the Cascade model [27]. A summary on the theoretical status is presented in the appendix of the PrimEx note #57 [28]. As such, the η width should be remeasured by the Primakoff process using state-of-the-art experimental techniques to resolve the discrepancy between the Primakoff and two-photon measurements. The proposed experiment will improve the previous Primakoff experiment in the following respects:

1. Use a tagged, high precision, high energy photon beam to control the photon flux and suppress the inelastic background. An untagged photon beam was used in previous Cornell experiment;
2. Choose a proton target to be free of the nuclear incoherent background and enable good separation of the Primakoff production mechanism from the nuclear coherent backgrounds.
3. Choose the simplest compact nuclear target ^4He with a four times larger primakoff cross section (compared to the proton) and a well known charge form factor.
4. More solid theoretical foundation for interpreting the results.

4 Measurement of the η Radiative Width via the Primakoff Effect

We propose to use a tagged photon beam and the GlueX standard experimental setup in Hall D to measure the width of the $\eta \rightarrow \gamma\gamma$ decay via the Primakoff effect. In the Primakoff effect, shown in figure 4, mesons are produced by the interaction of a real photon with a virtual photon from the Coulomb field of the nucleus. The formation of mesons will be identified through the invariant mass of the two decay photons from the $\eta \rightarrow \gamma\gamma$ reaction, and the meson production angles will also be reconstructed by detecting the η decay photons.

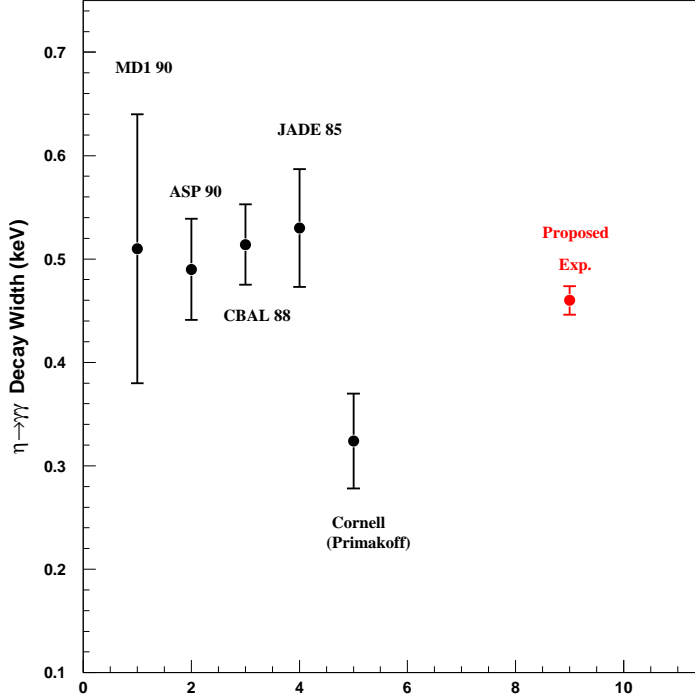


Figure 3: Two-photon decay width for the η meson. Points 1 through 4, are the results of e^+e^- collisions (for references, see [17]), point 5 is the result of a Primakoff experiment [22]. Point 6 is the expected error for proposed experiment with 3% total error, arbitrarily plotted to agree with the average value of previous five measurements. The plotted uncertainties combine the statistical and systematic errors in quadrature.

The production of mesons in the Coulomb field of a nucleus by real photons is essentially the inverse of the decay $\eta \rightarrow \gamma\gamma$, and the cross section for this process thus provides a measure of the η two-photon decay widths. For unpolarized photons, the Primakoff cross section on a zero-spin nuclear target is given by[29]:

$$\frac{d\sigma_P}{d\Omega} = \Gamma_{\gamma\gamma} \frac{8\alpha Z^2 \beta^3 E^4}{m^3 Q^4} |F_{e.m.}(Q)|^2 \sin^2\theta \quad (7)$$

where $\Gamma_{\gamma\gamma}$ is the decay width of the η , Z is the atomic number, m , β , θ are the mass, velocity and production angle of the mesons, E is the energy of the incoming photon, Q is the momentum transferred to the nucleus, and $F_{e.m.}(Q)$ is the nuclear electromagnetic form factor, corrected for final state interactions of the outgoing η .

The Primakoff effect is not the only mechanism for meson photoproduction at high energies. For a nuclear target there is coherent background from strong production of η in

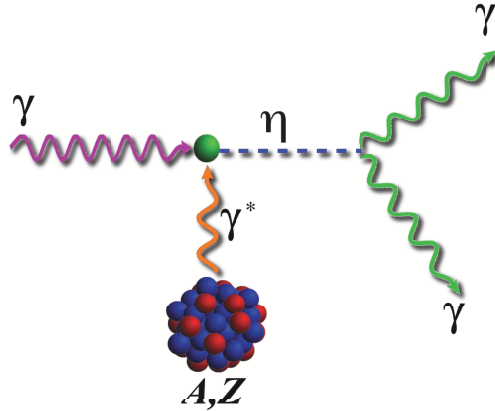


Figure 4: Schematic representation of the Coulomb photoproduction of neutral mesons (Primakoff effect).

the nuclear hadronic field, and an interference between the strong and Primakoff production amplitudes. The full cross section is given by:

$$\frac{d\sigma}{d\Omega} = \frac{d\sigma_P}{d\Omega} + \frac{d\sigma_C}{d\Omega} + \frac{d\sigma_I}{d\Omega} + 2 \cdot \sqrt{\frac{d\sigma_P}{d\Omega} \cdot \frac{d\sigma_C}{d\Omega}} \cos(\phi_1 + \phi_2) \quad (8)$$

where the Primakoff cross section, $\frac{d\sigma_P}{d\Omega}$, is given by equation (7). In the case of a nuclear target, the nuclear coherent cross section is given by:

$$\frac{d\sigma_C}{d\Omega} = C \cdot A^2 |F_N(Q)|^2 \sin^2\theta \quad (9)$$

and the incoherent cross section is:

$$\frac{d\sigma_I}{d\Omega} = \xi A (1 - G(Q)) \frac{d\sigma_H}{d\Omega} \quad (10)$$

where A is the nucleon number, $C \sin^2\theta$ is the square of the isospin and spin independent part of the neutral meson photoproduction amplitude on a single nucleon, $|F_N(Q)|$ is the form factor for the nuclear matter distribution in the nucleus (corrected for final state interactions of the outgoing mesons), ξ is the absorption factor of the incoherently produced mesons, $1 - G(Q)$ is a factor which reduces the cross section at small momentum transfer due to the Pauli exclusion principle, and $\frac{d\sigma_H}{d\Omega}$ is the η photoproduction cross section on a single nucleon. The relative phase between the Primakoff and nuclear coherent amplitudes without final state interactions is given by ϕ_1 and the phase shift of the outgoing meson due to final state interactions in the final state is given by ϕ_2 .

The classical method of extracting the Primakoff amplitude from the measured differential cross sections in the forward direction relies on the different characteristic behaviors

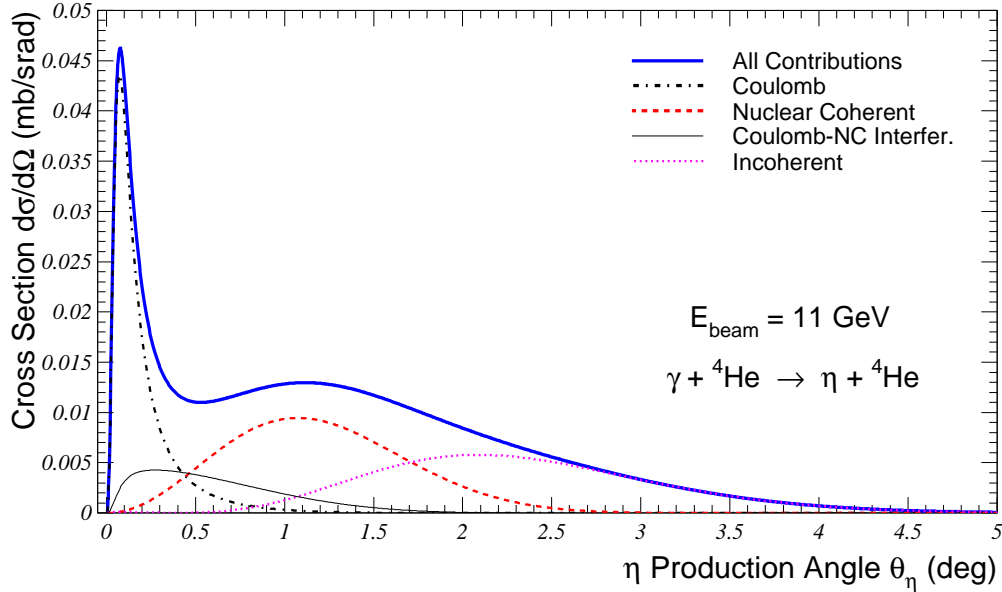


Figure 5: Differential cross sections (electromagnetic and nuclear) for the $\gamma + {}^4\text{He} \rightarrow \eta + {}^4\text{He}$ reaction in small angles at 11 GeV. The solid blue line is the total differential cross section from all processes; the dot-dashed black curve is from the Primakoff process; the dashed red curve is from the nuclear coherent process; the black line is from the interference between the Primakoff and nuclear coherent; and the dotted pink curve is from the nuclear incoherent process.

of the production mechanisms with respect to the production angle. For a spin zero target the Primakoff cross section is zero for mesons emitted along the incident photon direction, has a sharp maximum at a very small angle, and falls at larger angles as shown in figure 5 for a ${}^4\text{He}$ target. It is proportional to Z^2 , and its peak value is roughly proportional to E^4 . The nuclear coherent cross section for spin zero nuclei is also zero in the forward direction, but it has a broad maximum outside the angular region of the Primakoff effect, and falls at larger angles as shown in Figure 5. However, as can be seen from Figure 5, there are still two types of contributions under the Primakoff peak—the extended tail of the nuclear coherent mechanism, and the interference term between the two amplitudes as described above. The interference term amounts to a relatively large contribution and is also more difficult to identify since in addition to the knowledge of both amplitudes, it also requires knowing the relative phase angle between them. Therefore, a precision determination of the contribution from the background amplitudes under the Primakoff peak requires good experimental information on the nuclear amplitude outside of the Primakoff region. This can be experimentally achieved by using light nuclei as production targets. Since form factors for light nuclei fall slowly with momentum transfer, such targets are well suited for measuring the nuclear part at large angles, thereby determining the contribution under the Primakoff

peak.

As Figure 5 illustrates, compared to the Primakoff effect to produce a π^0 , η production has a significantly smaller cross section and peaks at relatively larger production angles. This is a consequence of the much larger mass of the η which increases the momentum transfer at a given production angle. As a result, the Primakoff peak is harder to distinguish from the nuclear background, as seen from Cornell group's result [22]. There are two ways to ameliorate this problem. One is to go to higher photon energies, which, in addition to increasing the Primakoff cross section ($\sigma_P \propto E^4$), will push the Primakoff peak to smaller angles ($\theta_{Primakoff} \sim \frac{m^2}{2E^2}$) as compared to those of the nuclear coherent effect ($\theta_{NC} \sim \frac{2}{EA^{\frac{1}{3}}}$). As such, the 12 GeV upgrade to the CEBAF accelerator is vital to these measurements. Another improvement is to use lighter targets such as ^1H , ^4He or ^{12}C which are more bound compared to heavier nuclei, thereby enhancing coherency. In addition, due to the A dependence just mentioned, one would expect the nuclear coherent mechanism to peak at larger angles for lighter nuclei, which helps to separate it from Primakoff production.

5 Choice of Primakoff Targets

We are proposing a measurement of the differential cross sections at forward angles on the proton and ^4He targets.

The theoretical simplicity of the proton target will essentially eliminate complicating factors for nuclear targets arising from nuclear incoherent amplitudes at low excitation energies and form factor distortion in a many-body nucleus. Ideally, one would like to measure recoil target nuclei to ensure coherency but, as illustrated in figure 6, the recoil kinetic energies involved are small. In this light, hydrogen is especially promising as a production target. The proton target has several advantages: (1) the incoherent hadronic contribution vanishes within our kinematical range; (2) the proton form factor is well known, and is free of corrections from the nuclear final state interactions; (3) the coherent hadronic photoproduction for proton is peaked at much larger angles than the Primakoff peak (see Figure 8). With a large experimental acceptance, we can experimentally measure the coherent hadronic photoproduction outside the Primakoff region, and then extrapolate the hadronic tail underneath the Primakoff peak; and (4) inspired by our 12 GeV Primakoff experimental program, the differential cross section of η photoproduction on a proton target in the forward angles has been recently calculated by J. Laget [31]. His results are shown in Figure 7 and 8 where the clean separation between the Primakoff and nuclear cross sections is evident. The Laget calculation for η photo-production on the proton utilizes the latest developments in the Regge description of the photoproduction of the π^0 in the strong field, and its extension into the η and η' sectors. The calculation reproduces all the available experimental data on the proton very well both at large and small production angles. It can also fix the relative sign of the Primakoff and nuclear coherent amplitudes. Based on the above arguments, the accuracy of the determination of the eta decay width is not sensitive to the errors and model assumptions in the hadronic process calculation, and proton is an excellent candidate as a Primakoff target.

It should be noted that a proof-of-principle exists for doing a Primakoff experiment on the proton. In the early 1970's a group at DESY measured forward π^0 photoproduction on the proton [32]. Their data clearly exhibit a Primakoff peak at forward angles, and the pion lifetime obtained from the data agrees, within quoted errors, with the accepted value.

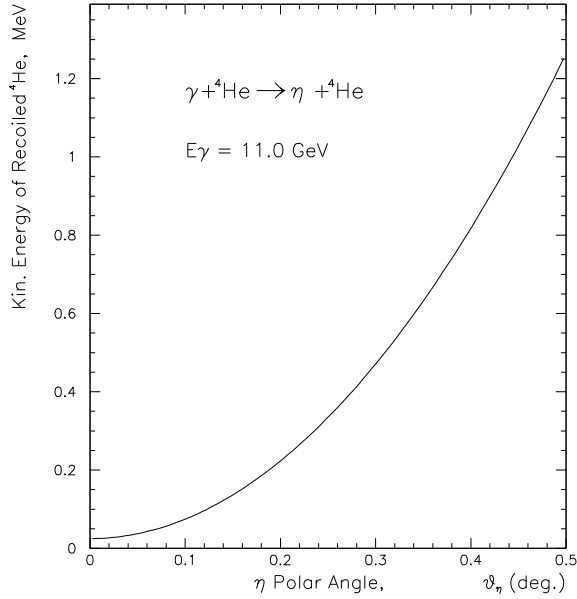


Figure 6: Recoil kinetic energy *versus* η production angle for ${}^4\text{He}$.

On the other hand, as the lightest compact nuclear target and having a better signal to noise ratio in the Primakoff region due to its four times larger Primakoff cross section than proton, as shown in Figure 5 and 8, ${}^4\text{He}$ is a strong candidate for Primakoff target as well. First, it is a very compact nucleus (with a nucleon threshold of ~ 20 MeV), which will favor coherent production. Second, its form factor is very well known and falls slowly with momentum transfer, which helps in extracting the nuclear coherent amplitude outside of the Primakoff peak precisely. In addition, it is a spin zero nucleus, which will largely suppress the spin flip amplitude contribution close to zero degrees. In addition, the final state interaction in ${}^4\text{He}$ is minimal and the theoretical calculations required for nuclear Primakoff experiments on ${}^4\text{He}$ target have been extensively studied recently [25]-[26]. The proton and ${}^4\text{He}$ targets are complimentary. Combined data on both targets would allow us to check the Z dependence of the Primakoff cross section which should be proportional to Z^2 . This approach was very successful in the *PrimEx I* experiment for the π^0 radiative width, where we took data on both ${}^{12}\text{C}$ and ${}^{208}\text{Pb}$ targets.

We argue that by simultaneously going to higher photon energies and using the light Primakoff production targets, proton and ${}^4\text{He}$, one can make clean measurements of the η decay width.

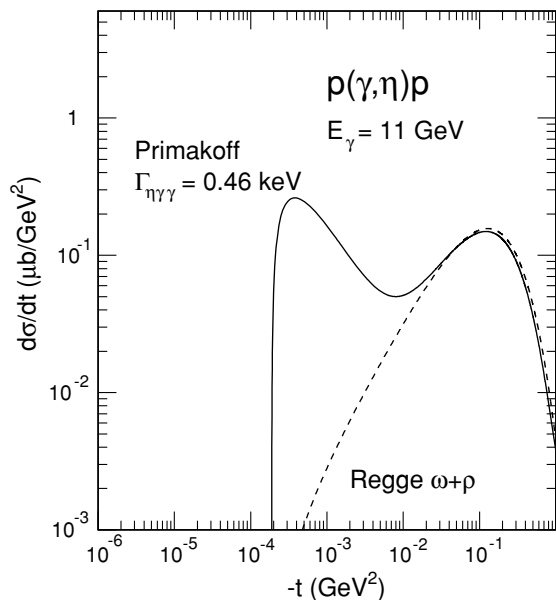


Figure 7: Differential cross section of the coherent η photoproduction on the proton as a function of the squared four-momentum transfer t . The dashed curve corresponds to the hadronic cross section, while the solid curve corresponds to the sum of the Primakoff and the hadronic amplitudes [31].

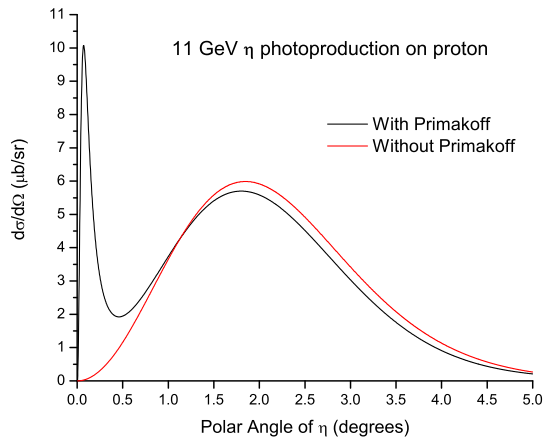


Figure 8: Differential cross section of the coherent η photoproduction on the proton as a function of the η production angle [31].

6 Experimental Setup

We propose to use a 10.5–11.7 GeV tagged photon beam in Hall D to produce the η mesons, and the two decay photons from the η will be detected by the forward calorimeter (FCAL) located ~ 5.6 m downstream of the target. As shown in Figure 9, the standard GlueX experimental setup with an additional small calorimeter (32.8×32.8 cm²) will be used in proposed experiment which includes: (1) a high energy photon tagger; (2) a pair spectrometer for photon flux monitoring; (3) a 30 cm length liquid hydrogen and ⁴He target; (4) a forward multichannel electromagnetic calorimeter (FCAL); (5) a 32.8×32.8 cm² PbWO₄ crystal calorimeter with 17 charge particle veto counters for Compton scattering detection (CompCal) which will be located 4 meters downstream of FCAL. During the η production run, the GlueX solenoid magnet will be turned off in order to detect the Compton scattering photon and recoiled electron in two calorimeters (FCAL and CompCal) simultaneously to check the setup stability, monitor the luminosity and FCAL detection efficiency, and verify the overall systematic errors in absolute cross section measurement. A 5 mm diameter collimator will be used in order to have a higher photon tagging efficiency and better control of photon flux. A 10^{-4} radiation length metal radiator will be used to ensure the stability of the photon flux at the end of the bremsstrahlung spectrum. Details of this instrumentation are

given below.

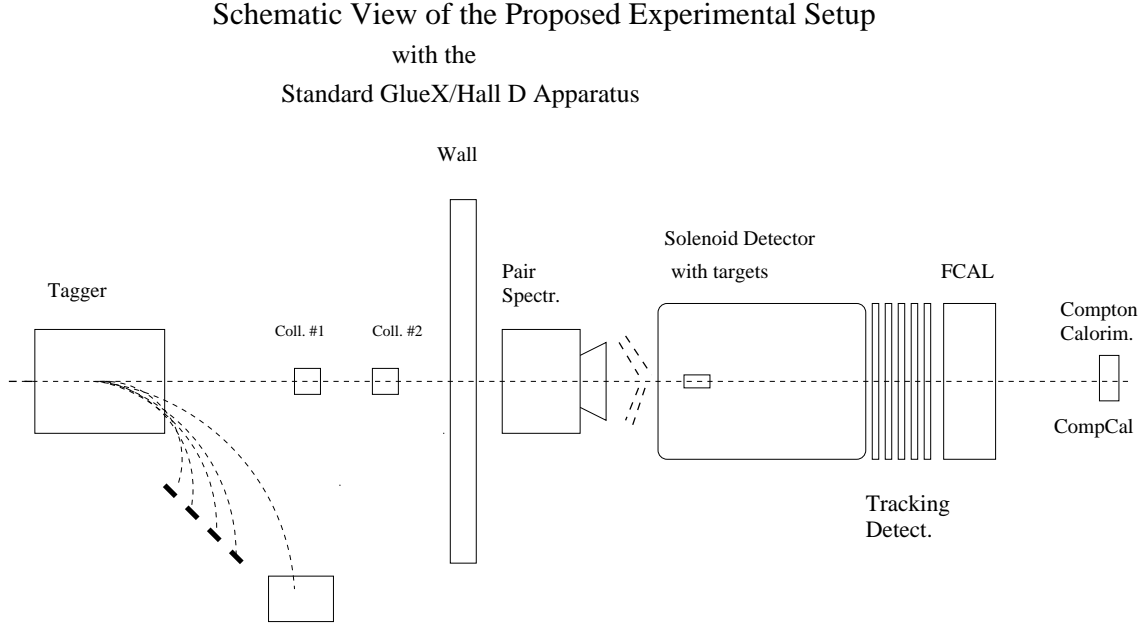


Figure 9: Top view of the experimental setup for η two-gamma decay width measurements. This includes: (1) a high energy photon tagger; (2) a pair spectrometer; (3) a physics target; (4) the FCAL calorimeter; (5) the CompCal calorimeter.

6.1 High Energy Photon Tagger

Jefferson Lab is in the process of designing and developing a tagged photon beam at 12 GeV in Hall D. While details of the design can be found in reference [33], the main features of the current design are:

1. Photon energy detection from 70% to 75% of the primary electron beam energy with energy resolution of about 0.5% (r.m.s.) of the primary beam energy. A detector system which allows a counting rate of at least 5×10^6 electrons per second per 0.1% energy bin over this range of photon energies.
2. An additional capability for photon energy detection from 25% to 97% of the primary electron beam energy. It will be capable of pre-collimated intensities up to 150MHz/GeV, with 50% sampling of 60 MeV energy bins below 9 GeV and full coverage with 100% sampling of 30 MeV wide energy bins above 9 GeV photon energy.

The tagging spectrometer is an Elbek-type spectrometer. The 12 GeV electrons pass through the radiator target where a small fraction undergo bremsstrahlung. The electrons then pass through a focusing quadrupole and are bent by the 6 meters tagger magnet. The

majority of the electrons which did not interact with the radiator are bent 13.4° and then propagate straight to the electron beam dump. A large vacuum vessel is integrated into the magnet and extends out to the spectrometer focal plane so only the small amount of multiple scattering inside the radiator and in the exit window effect the resolution. The spectrometer detectors are positioned immediately outside the focal plane to determine the momentum of electrons that produce bremsstrahlung photons. The photon energy, E_γ , is determined by the difference between the initial electron beam energy and the energy of the post-bremsstrahlung electron deflected towards the focal plane.

The detector package is divided into two parts: (1) a set of 190 fixed scintillation counters spanning the photon energy range from 3.0 to 11.7 GeV, and (2), a movable “microscope” of 500 scintillating fibers optimized for coherent photon beam operation spanning the energy range from 8.3 to 9.1 GeV. The fixed array provides access to the full tagged photon spectrum, albeit at a modest energy resolution of $\sim 0.1\%$ and reduced rate capability. These detectors are well suited for running with a broadband incoherent bremsstrahlung source. The microscope provides energy resolution better than 0.07% in order to run in coherent mode at the highest polarization and intensities. Using the microscope, the source is capable of producing collimated photon spectral intensities in excess of 2×10^8 photons/GeV, although accidental tagging rates will limit normal operation to somewhat less than this.

For the proposed η radiative decay width measurement, we will use an incoherent bremsstrahlung photon beam in an energy range from 10.5 GeV to 11.7 GeV. The current design of the fixed scintillation counters in this energy range with 30 MeV wide energy bins is sufficient for this measurement. We will require a 112 nA electron beam on a 10^{-4} radiation length metal radiator. It will provide a 7×10^7 equivalent photons/sec on the physics target after passing through a 5 mm diameter primary collimator.

Beam Collimation and Position Stability

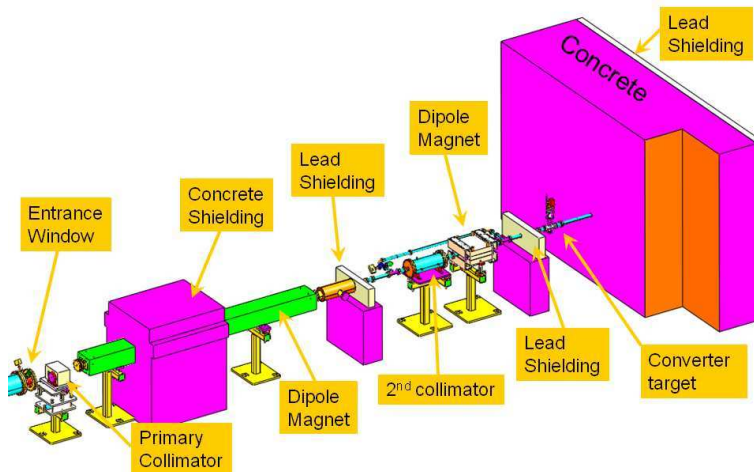


Figure 10: The layout of the collimator cave.

For polarized photon experiments, a 12 GeV electron beam interacting with a 20 μm diamond radiator produces the photon beam. The characteristic opening angle for bremsstrahlung photons is $m_e/E = 42 \mu\text{rad}$. After 76 meters of drift in vacuum the photon beam enters in the collimator cave from the left through a thin 250 μm Kapton window 8'' (203mm) in diameter and immediately interacts with the primary collimator. The layout of the collimator cave is shown in figure 10. The primary collimator consists of two main components: an active collimator which measures the centroid of the photon beam and a hybrid tungsten lead passive collimator. The size of the passive collimator is 3.4 mm in diameter for the GlueX run. However, we will use a larger collimator size of 5 mm in diameter for the η decay experiment in order to double the photon tagging efficiency and ensure the photon flux control at 1% level. The active collimator is electrically isolated, has an inner aperture of 5 mm, and is precisely mounted in front of the primary collimator. The purpose of the active collimator is to measure the position of the centroid of the photon beam with an accuracy of 200 μm . The tungsten passive collimator is surrounded by 8'' of lead for additional shielding. A large flux of particles are generated in the passive collimator and some lie along the photon beam. A sequence of sweeping magnets after the collimator removes the unwanted particles from the photon beam. A second collimator is located following the lead shielding wall of the first collimator. This collimator is made of stainless steel and is 20'' long and 8'' in diameter. A 1 cm hole is bored along the axis of the collimator and is designed so that the effective aperture can be adjusted to 6, 8, or 10 mm by inserting stainless steel tubes in the collimator aperture. The purpose of this collimator is to scrape off photons which were produced by low angle scattering on the bore of the primary collimator. A second sweeping magnet is mounted directly after the second collimator.

The specification of the tolerance on this alignment during beam operation is a circle of radius 200 microns. The size of the beam spot on target is defined by the primary collimator. As shown in figure 11, if the beam centroid is aligned within 200 microns, the deviation of the photon flux on the target can be controlled within 1% for a 5 mm in diameter primary collimator.

6.2 Pair Spectrometer

The most important diagnostics for the photon beam flux are the count rates in the tagger's fixed hodoscope array and the microscope. By detecting the electrons which underwent the bremsstrahlung interaction, one determines precisely the energy spectrum of the photon beam in front of the collimators. The photon flux on the target, however, is only a fraction of the tagged photons because of the collimation. The absolute photon flux on the target will depend strongly on the exact details of the collimation. It is proposed to use pair production which is a well understood QED process as the basis for the relative photon flux determination. An additional calibration measurement is needed to determine the pair spectrometer's absolute efficiency. This is done with dedicated calibration runs at low beam intensity with a total absorption counter (lead glass) inserted in the beam after the spectrometer.

The layout of the proposed pair spectrometer is shown in Figure 12. It consists of a thin foil converter (1×10^{-3} radiation length thick) placed in the photon beam after the last collimator (at 0.5 m distance upstream of the front end of the pair spectrometer magnet)

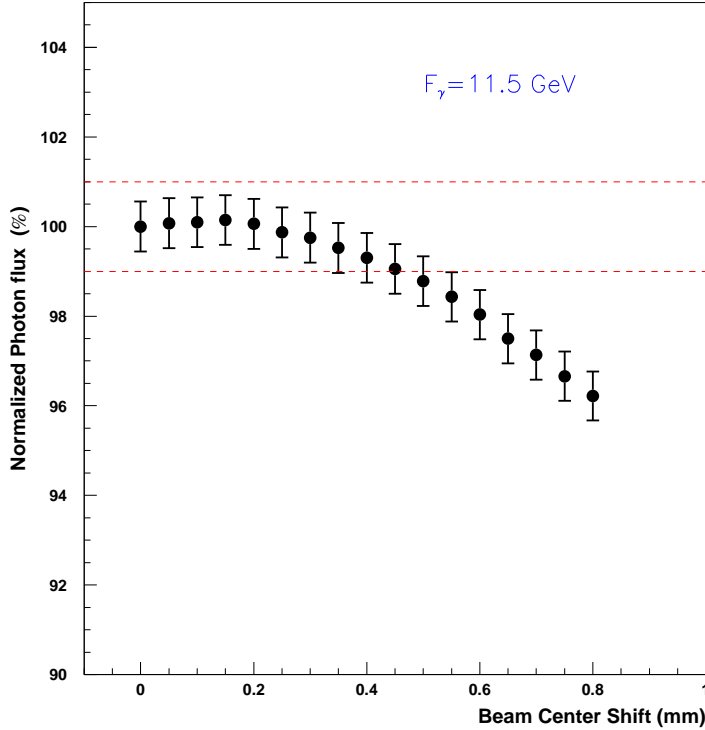


Figure 11: Results from Monte Carlo studies of photon flux stability for a 5 mm diameter primary collimator. It shows the normalized photon flux after the collimation as a function of the offset of the beam centroid from the collimator axis. The dashed lines show $\pm 1\%$ deviation from the photon flux when the beam centroid has a zero offset.

to generate electron/positron pairs through pair production. The electrons and positrons produced in the converter are swept away from the photon beam in a strong dipole field (1.64 T) and are subsequently detected by the coincidence of hits in the front and back arrays of scintillator hodoscopes. The photon energy is then simply the sum of the electron and positron energies. The current pair spectrometer detector package design is asymmetrical and consists of a total of 42 counters. On the positron side the Fine Spacing Forward (FSF) hodoscope will consist of 24 close-packed scintillator counters measuring momenta between 3 and 4 GeV/c in equally spaced momentum bins. The momentum uncertainty per bin is 12 MeV. On the electron side the Wide Spacing Forward (WSF) hodoscope is a sequence of six narrow scintillators covering the range 3.25 to 8.25 GeV/c. The momentum uncertainty per bin is 17 MeV. There are an additional four Fine Spacing Backward hodoscopes (FSB) in the positron arm and six Wide Spacing Backward hodoscopes (WSB) in the electron arm used for triggering purposes. A coincidence between one counter in the FSF and one in the WSF corresponds to one photon energy bin. This arrangement gives $6 \times 24 = 144$ photon momentum bins equally spaced in energy between 6.25 GeV and 12.25 GeV with a nominal

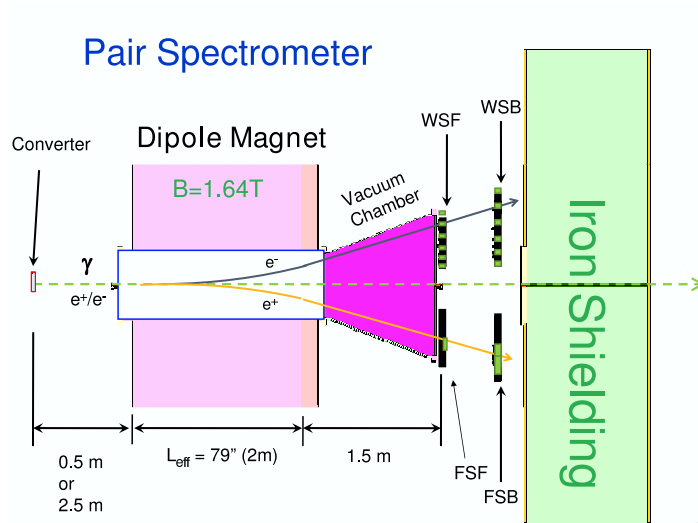


Figure 12: Layout of the pair spectrometer in Hall D. On the left is a thin 10^{-3} radiation length converter followed by a strong spectrometer magnet. The vacuum chamber extends beyond the end of the magnet to the front of the first hodoscope plane. The first scintillator hodoscope is placed 1.5 m beyond the end of the magnet. A second hodoscope plane is placed 0.8 m behind the first plane and is used for triggering.

21 MeV uncertainty per bin. This spectrometer design provides uniform acceptance over the energy range from 6.25 GeV to 12.25 GeV using a minimum number of counters. The detailed design can be found in reference [33].

The proposed η experiment will use the incoherent photon beam at the highest possible energy ($E_\gamma=10.5\text{--}11.7$ GeV). The UNCW group (one of the leading groups in the Primakoff team) has been working on Monte Carlo simulation to cross examine the current design in order to ensure that the pair spectrometer would be an effective tool to control the absolute photon flux at the 1% level.

6.3 Targets

We propose to use the standard Hall D liquid hydrogen and ^4He targets with 30 cm in length, corresponding to approximately of 3.46% radiation lengths for hydrogen and 3.99% for ^4He .

Hall D is planning to use a cryogenic target system similar to what has been developed for Hall B [34]. While some details of the Hall D target system are still undefined, the main element of the cryogenic target is a heat exchanger in contact with the target that is refrigerated down to 2.5 K by pumping liquid helium through a Joule-Thompson valve. Experience in Hall B has shown that after a 15-liter buffer cryostat has been filled from the torus, oscillations in the target temperature are smaller than ± 0.02 K [35]. The Hall B g10a target cell, with design similar to that proposed for use in Hall D, is 24 cm in length. The upstream end of the target has an inner diameter of 5.51 cm, tapering down to 4.0 cm inner

diameter on the downstream end of the target. The reason for the taper is to eliminate dead zones in the target, where cooling is limited. The radius on the endcaps is 4 cm. The target cell is constructed from 5 mil kapton.

One important issue for a cryogenic target is the target density. Since target vaporization does not occur for a real photon beam, the target density can be deduced from the equation of state and the target pressure-temperature data. This has been performed in detail for the CLAS G1C run period, and the uncertainties in the average hydrogen densities for G1C runs were estimated at $\pm 0.14\%$ [36]. During the proposed experiment, target temperatures and pressures will be written into the data stream.

The effective target length depends on the photon beam spot size, the target offset, and angle relative to the beam. These effects were carefully studied for the CLAS G1A run period [37]. In the G1A analysis the largest systematic error in the effective target length was estimated to result from an offset of the target from the scattering center. In the early days of Hall B running the target offset was estimated to be as large as 5 mm. This caused a systematic uncertainty in the effective target length of 1 mm for G1A running.

To make an estimate for the uncertainty in the effective target length for the Hall D experiment, we made the following assumptions:

- Target length of 30 cm, with endcap of 2.5 cm in diameter.
- Beam spot sigma of 1.5 mm (5 mm collimation 20 m from the target).
- Target-center offset no greater than 1 mm.
- Target-front offset from target-back no greater than 1 mm.

If the target offsets can be held to the level of 1 mm, then the uncertainty in the effective target length is dominated by the uncertainty in measuring the target length, which is estimated at ± 0.2 mm [37]. This gives a fractional error in the effective target length of $\pm 0.07\%$.

In summary, during the experiment we propose to carefully monitor the cryogenic target pressures and temperatures, and continually write these variables into the event stream. Based on experience running similar targets in Hall B, we expect that the target density can be monitored at the level of $\pm 0.14\%$. The target position should be surveyed in with a precision of ± 1 mm, giving an error of $\pm 0.07\%$ for the effective target length. With these conditions, we estimate that the total uncertainty in the cryogenic target area density can be held at the level of $\pm 0.16\%$.

6.4 Forward Electromagnetic Calorimeter (FCAL)

At the incident photon energies of this experiment ($E_\gamma=10.5\text{--}11.7$ GeV), the Primakoff cross section peaks at extremely small angles ($\theta_{peak} \simeq 0.2^\circ$). Therefore, in order to extract the Primakoff amplitude from the competing nuclear background, the experimental setup must have sufficient angular resolution for detecting forward produced η 's which are

identified by detecting the decay photons ($\eta \rightarrow \gamma\gamma$) in the multi-channel electromagnetic calorimeter. Good total energy and invariant mass resolutions in the $\gamma\gamma$ system are also required for the selection of coherent η production from the experimental background. These kinematic variables have strong dependence on both the position and energy resolutions of the calorimeter. In addition, the kinematic constraints imposed by the knowledge of the initial photon energy provided by the tagging system results in a significant improvement of the angular resolution and invariant mass. The combination of the photon tagging facility and a high resolution electromagnetic calorimetry is one of the important advantages of our experiment over the previous Primakoff type of experiments. It provides significantly improved invariant mass resolution for the clean identification of the η 's and a high resolution in the η production angle for extracting the Primakoff amplitude from the competing background nuclear processes.

We propose to use the standard GlueX forward electromagnetic calorimeter (FCAL) for the η experiment. The FCAL consists of 2800, $4 \times 4 \times 45$ cm³ lead glass blocks stacked in a 2.4 m diameter circular array. The radiation-hard F108 type glass will be used in the central region about 30 cm radius, while the F8-00 type glass will be used in the outer region. A central 12×12 cm² hole is left open to enable the photon beam to pass through. Each block will be optically coupled to an FEU 84-3 PMT which will be instrumented with flash ADC electronics. The projected energy resolution of FCAL is $\sigma_E/E = 5.8/\sqrt{E} \oplus 1.3$ percent for F108 glass and $\sigma_E/E = 5.5/\sqrt{E} \oplus 0.8$ percent for F8-00 glass. The position resolution for both types of glass is estimated to be $\sigma_p(\text{cm}) = 0.64/\sqrt{E}$. The detail of the FCAL design can be found in Hall D web site.

6.5 Compton Calorimeter (CompCal)

In addition to the standard GlueX experimental setup, we suggest to add a small 32.8×32.8 cm² PbWO₄ crystal calorimeter to measure the atomic electron Compton cross section in parallel to the η production run. The Justification for the need of CompCal is described later in the Section 10. This device will provide an independent verification on the overall systematic errors of the experimental setup, including luminosity, the FCAL detection efficiency, and experimental stability. The CompCal will consist of 16×16 matrix of PbWO₄ crystal array. Each module has a dimension of $2.05 \times 2.05 \times 18$ cm³. Based on our previous experience working on the PbWO₄ hybrid calorimeter (HYCAL) in Hall B, the PbWO₄ crystal calorimeter not only provides higher energy and position resolutions but also significantly improves the radiation hardness of the detector near the beam line where the radiation doses are higher. During the *PrimEx I* running period, HYCAL (with only a 4.1×4.1 cm² beam hole) was in the beam for more than three months under the condition of luminosity 7×10^7 equivalent γ 's/sec on a 5% r.l. target. By comparing the calibration data taken at the beginning and end of the experiment, the changes of gain for 2000 channels are less than a few percent. As a result, we plan to have a central 4.1×4.1 cm² beam hole in the CompCal following the same design as the HYCAL. Similar to the HYCAL, the most inner layer of crystal modules around the beam hole will be covered with ~ 12 R.L. of Tungsten in order to be protected from high radiation dose, while those modules are still included in the energy

and position reconstruction. There are 17 scintillating charge particle veto counters in front of the CompCal for offline data analysis. Each veto counter has a dimension of 2 cm wide, 33 cm high, and 1 cm thick. We will build CompCal with same type of PbWO_4 crystal as the HYCAL. The energy resolution of CompCal is $\sigma_E/E = 2.3/\sqrt{E} \oplus 0.8$ percent and the position resolution is $\sigma_p(\text{cm}) = 0.25/\sqrt{E}$.

7 Acceptance, Resolutions and Event Selection

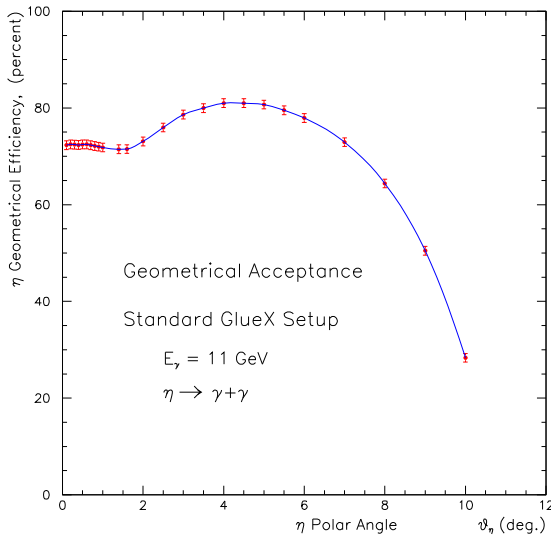


Figure 13: Geometrical acceptance of FCAL calorimeter *versus* η production angle.

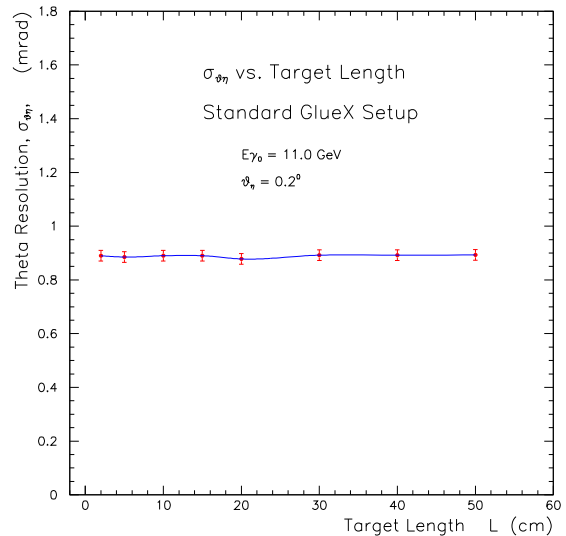


Figure 14: Expected resolutions in θ_η for different target lengths. The collimator diameter is fixed at $D = 5$ mm for these simulations.

The extraction of $\eta \rightarrow \gamma\gamma$ decay width via the Primakoff method, as it is discussed in Section 4, requires a measurement of forward differential cross sections of η coherent photo-productions with a high precision. To achieve this goal, one needs (1) the knowledge of geometrical acceptance and detection efficiency, (2) experimental resolutions of the kinematical parameters, and (3) effective event selection.

7.1 Geometrical Acceptance

The geometrical acceptance defines the solid angle in the experiment and any errors in this parameter directly propagate into final systematic errors of measured cross sections. The error in this quantity comes from the geometrical uncertainty of the experimental setup and mostly position resolutions of the detectors used in the experiment. In the proposed experiment we reconstruct the physics event through measurement of two decay photons

in FCAL, the energy and direction of the incident photon. Therefore, the following items are included in the calculation: (1) the beam direction and its position on target, (2) the position and length of the target, (3) the position and geometry of the FCAL calorimeter, (4) the position resolution of FCAL, and (5) the material between target and FCAL.

Figure 13 shows the Monte Carlo simulation result of geometrical acceptance versus η production angle for the incident photon beam energy at 11 GeV. A relatively large size of the FCAL located at 5.6 m distance from the target provides a good and rather smooth geometrical coverage (about 70%) for the forward production angles. Our study also indicates that the error on the geometrical acceptance can be controlled at less than 0.5% level as shown in Table 2.

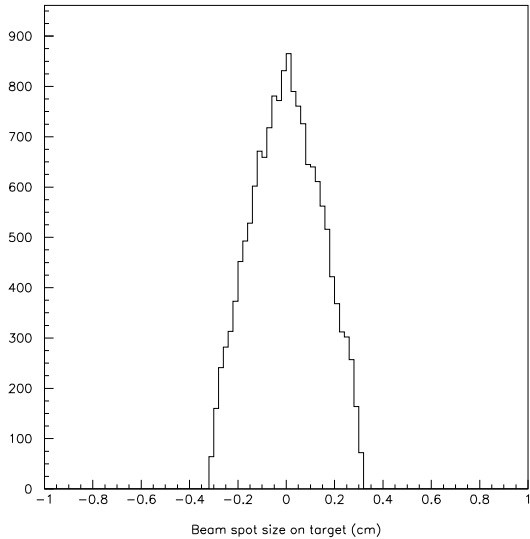


Figure 15: The x distribution of the interaction vertex in the target for a collimator diameter $D = 5\text{mm}$.

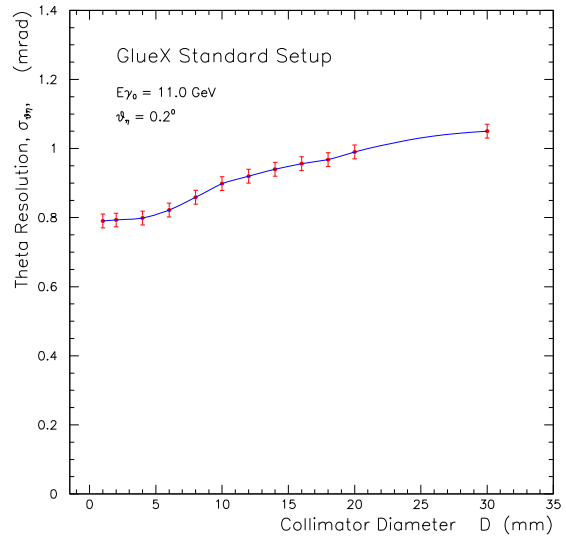


Figure 16: FCAL θ_η resolution *versus* collimator diameter.

7.2 Experimental Resolutions

The experimental resolutions for the measured and calculated kinematical variables are extremely important in the event selection and cross section measurement. It is also crucial in the final stage to extract the η decay width by fitting the measured differential cross sections.

Resolution in θ_η is of particular importance in the identification of the forward peaked η 's photoproduced by the Primakoff mechanism ($\theta_\eta \sim 0.2^\circ$) from η 's produced at larger angles via the nuclear coherent process by fitting the angular distribution of η photoproduction. The η production angle can be determined from the measured photon energies and angles by:

$$\cos\theta_\eta = \frac{E_{\gamma 1}\cos\theta_{\gamma 1} + E_{\gamma 2}\cos\theta_{\gamma 2}}{\sqrt{E_{\gamma 1}^2 + E_{\gamma 2}^2 + 2E_{\gamma 1}E_{\gamma 2}\cos\psi_{\gamma 1\gamma 2}}}. \quad (11)$$

where $E_{\gamma i}$ and $\theta_{\gamma i}$ ($i = 1, 2$) are the energy and scattering angle of photons, $\psi_{\gamma 1\gamma 2}$ is the opening angle between the two photons.

To determine the photon angles, the vertex of the reaction in the target is required. Unfortunately, in this experiment we can not detect the recoil particles due to their small recoil energies (see Figure 6). The unknown z -position of the interaction vertex in the target will contribute to the experimental resolutions of the reconstructed production angle. Figure 14 shows the expected θ_η resolution for different target lengths. As it is clearly seen, the 30 cm cryogenic target planned for the GlueX setup can be used in the proposed experiment.

By similar arguments, the beam spot size at the target could be potential limiting factor of the θ_η resolution. The size of the beam spot is directly correlated with the size of the primary collimator in the beam line. For illustration, Figure 15 shows the beam spot x projection on the target for a $D = 5$ mm collimator size. Figure 16 shows the calculated angular resolution as a function of the photon beam collimator diameter. As one can see, our choice of a collimator size of $D = 5$ mm diameter for the η experiment will still provide a resolution in the production angle reasonably small, while improve our capability to control the photon flux as discussed in Section 6.1. Figure 17 show the θ_η angular resolutions reconstructed from FCAL near the Primakoff peak region; and Figure 18 show the θ_η angular resolutions near the nuclear coherent peak region. The production angular resolution is about ~ 1.1 mrad near the Primakoff peak region and is about ~ 1.3 mrad near the nuclear coherent peak region. Figure 19 and Figure 20 are the η energy resolutions measured by FCAL with and without kinematical fit [38]. It demonstrates that the kinematical fit will improve the energy resolution by $\sim 35\%$.

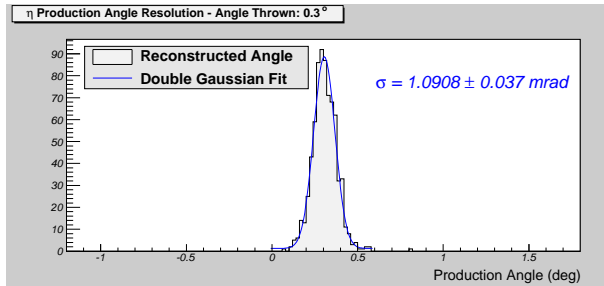


Figure 17: The θ_η resolution reconstructed from two photons detected by FCAL near Primakoff peak region.

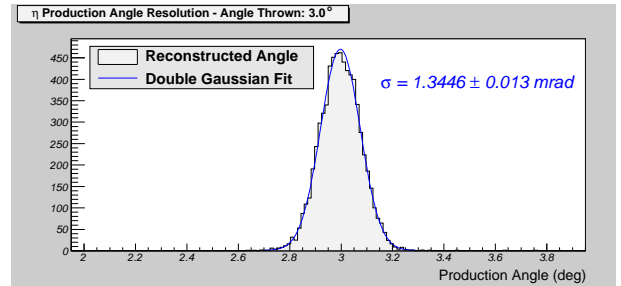


Figure 18: The θ_η resolution reconstructed from two photons detected by FCAL near nuclear coherent peak region.

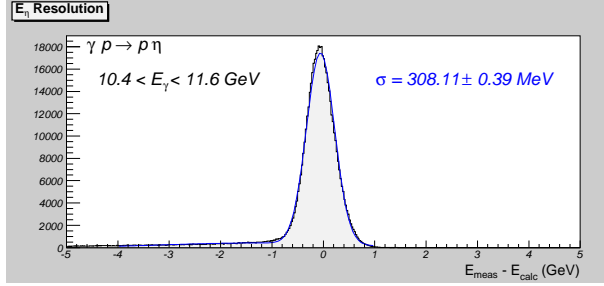


Figure 19: The E_η energy resolution reconstructed from two photons detected by FCAL without kinematical fit.

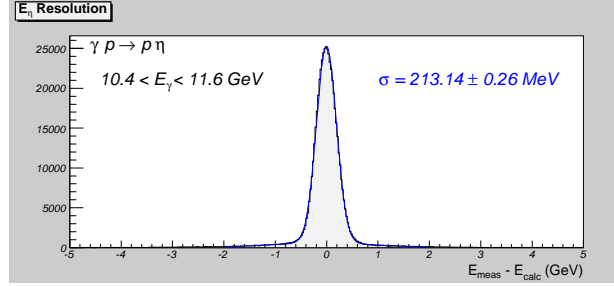


Figure 20: The E_η energy resolution reconstructed from two photons detected by FCAL with kinematical fit.

7.3 Event Selection

To select $\gamma + A \rightarrow \eta + A$ (where A is p or ${}^4\text{He}$) elastic events from the experimental data, we will apply the following event selection criteria: (1) the fiducial size of FCAL (excluding the most inner and outer layer modules of FCAL); (2) timing cut between the photon tagger and FCAL; (3) total energy deposited in FCAL; (4) the invariant mass reconstructed from the two decay photons to be the mass of η ; (5) energy conservation in the reaction (the elasticity cut); (6) missing mass to be the mass of target particle (p or ${}^4\text{He}$).

The cut on the total energy deposited in the FCAL is one of the effective ways to filter out the multichannel background reactions and accidental beam related background from the inelastic channels. Figure 21 and Figure 22 are the distributions of total energy deposited in FCAL from the elastic reaction $\gamma p \rightarrow \eta p$ and one of the major inelastic background reaction respectively. As one can see, for the beam energy in 10.4–11.6 GeV range, an 8.5 GeV threshold on FCAL total energy effectively selects the signal events, and removes significantly the events from the background processes.

The two photon invariant mass criteria will effectively distinguish the signal events from the accidental and combinatorial backgrounds. It can be defined directly from the momentum of two decay photons (the energies and positions of two decay photons detected by FCAL and the center of the target). In order to study the GlueX magnetic field effect, the invariant mass resolution of 2γ system ($\eta \rightarrow \gamma\gamma$) reconstructed by FCAL are shown in Figure 23 and Figure 24 for the GlueX magnetic field on and off. As one can see in Figure 23, there is a long tail on one side of invariant mass spectrum with magnetic field on caused by the loss of cluster energy due to the secondary charged particle from the η decay photons being bent away in the magnetic field. The resolution of invariant mass can be further improved by applying the kinematical fits [38].

The energy conservation in the reaction can be defined by two equivalent ways. One is defined by the difference between beam energy and the energy sum of two photons corrected by the recoil kinetic energy of target particle. In the case of ${}^4\text{He}$ target, the recoil energy is very small and can be ignored. The second way to define the elasticity is the missing mass calculated by the incident beam energy and the momentum of two decay photons to be the mass of the target particle. Figure 25 show the elasticity defined by the energy difference,

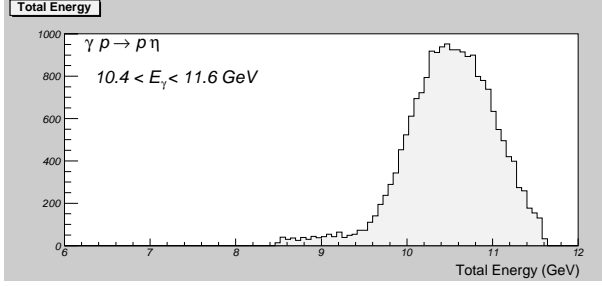


Figure 21: Distribution of the energy sum deposited in FCAL for elastic channel $\gamma p \rightarrow \eta p$.

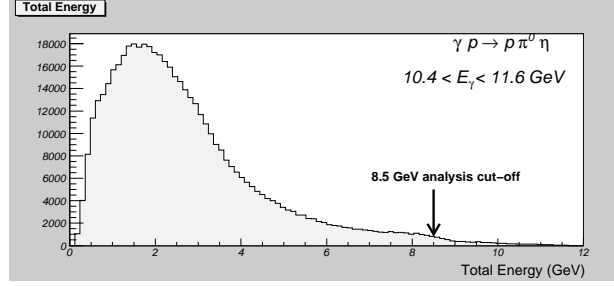


Figure 22: Distribution of the energy sum deposited in FCAL for background channel $\gamma p \rightarrow \eta \pi^0 p$.

with approximately 260 MeV resolution, but can be improved by a factor of 2 by using the η mass and the opening angle constraint. Figure 26 show the square of missing mass distribution for the proton target, it is peaked at proton mass square with a resolution of 370 MeV^2 . Figure 27 is a 2-dimensional histogram for the invariant mass vs. missing mass square from elastic signal reaction $\gamma p \rightarrow \eta p$; and Figure 28 is the same distribution from the inelastic background channel $\gamma p \rightarrow \pi^0 \eta p$. As one can see, the missing mass cut can effectively remove the background reaction from the data sample.

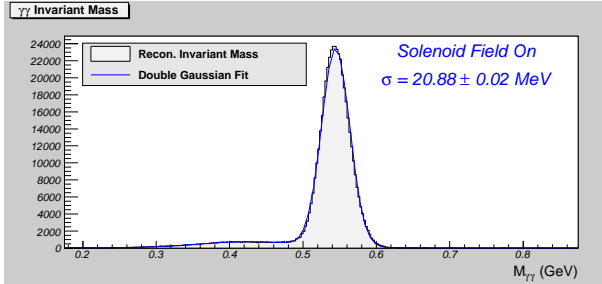


Figure 23: The invariant mass of 2γ detected by FCAL with magnetic field on.

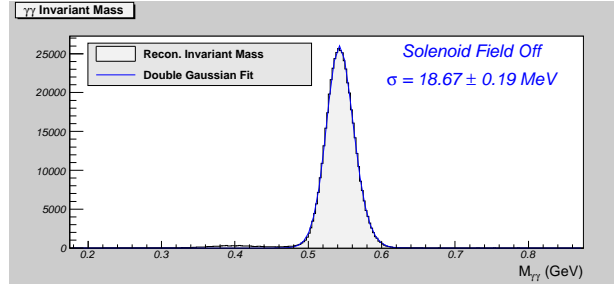


Figure 24: The invariant mass of 2γ detected by FCAL with magnetic field off.

8 Background Simulation

There are several types of backgrounds that need to be considered, as well as their impact on the final extraction of the Primakoff signal. The signal of interest consists of the exclusive $\gamma p \rightarrow \eta p$ reaction, followed by the decay of $\eta \rightarrow \gamma\gamma$. The extraction of the η radiative decay width from this reaction is treated in other sections (see Section 4 and 9.2). In this section we discuss interactions that might mimic the signal reaction, and must be removed from the data sample using specific event selection cuts, or measured over kinematics where they can be distinguished from the signal and subtracted from the data sample. We consider the following backgrounds and discuss how they affect the final measurement:

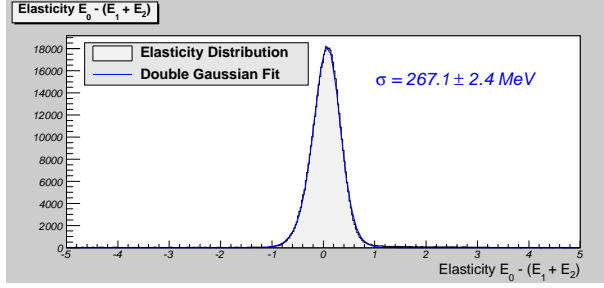


Figure 25: The elasticity defined by the difference of beam energy and energy sum of 2γ detected by FCAL corrected by the recoil kinetic energy of proton.

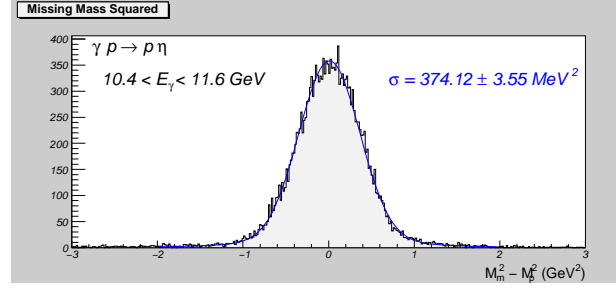


Figure 26: The square of missing mass distribution for $\gamma p \rightarrow \eta p$ reaction.

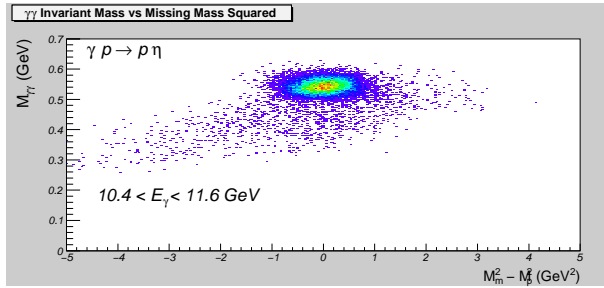


Figure 27: Invariant mass vs. Missing mass distribution for elastic $\gamma p \rightarrow \eta p$ reaction.

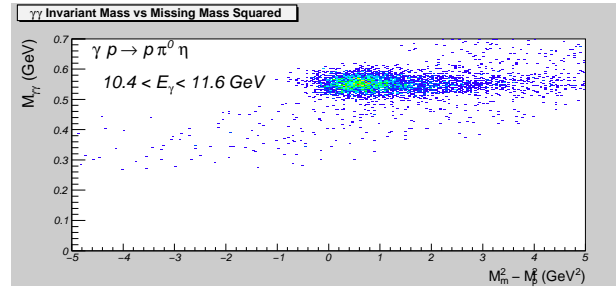


Figure 28: Invariant mass vs. Missing mass distribution for $\gamma p \rightarrow \pi^0 \eta p$ background reaction. The cut for η being detected by FCAL is applied.

1. electromagnetic and hadronic interactions that do not produce an η in the final state, such as $\gamma p \rightarrow \gamma \gamma p X$, but deposit energy in the detector that, when combined in random coincidence with other particles, mimic the reaction of interest.
2. hadronic interactions with an η in the final state, of the type $\gamma p \rightarrow \eta p X$ events. These include the following reactions: $\gamma p \rightarrow \eta \pi^0 p$ and $\gamma p \rightarrow \eta \pi^+ n$.

The signal reaction is identified by two photons, with an invariant mass of the η meson, in coincidence with an incident photon in the energy range of 10.5–10.7 GeV. Furthermore, as described earlier, the energy of the reconstructed η will carry essentially all of the energy of the incident photon as well as have a direction within a few degrees of the beam direction. We note that the recoil proton will have such a low energy that most of them will be stopped in the target and not detected. For the first type of backgrounds, the timing spread between signals can be used to remove them from the reaction of interest.

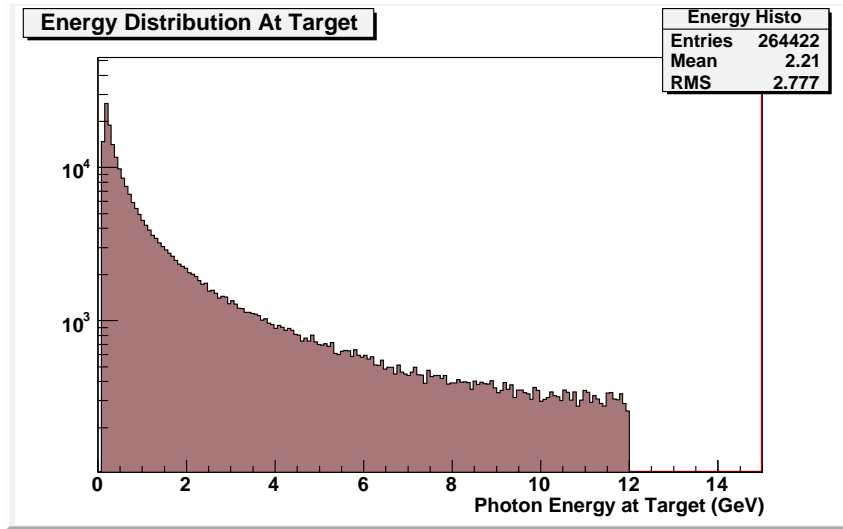


Figure 29: Distribution of the photon beam energy on the target.

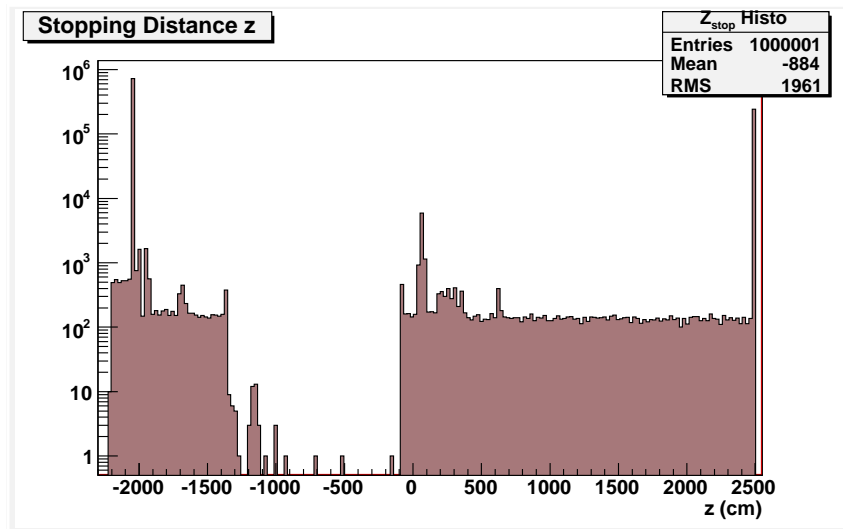


Figure 30: The z distribution of the background originated along the beam line. The primary collimator is located at $z = -2050$ cm and the target is at $z = 65$ cm.

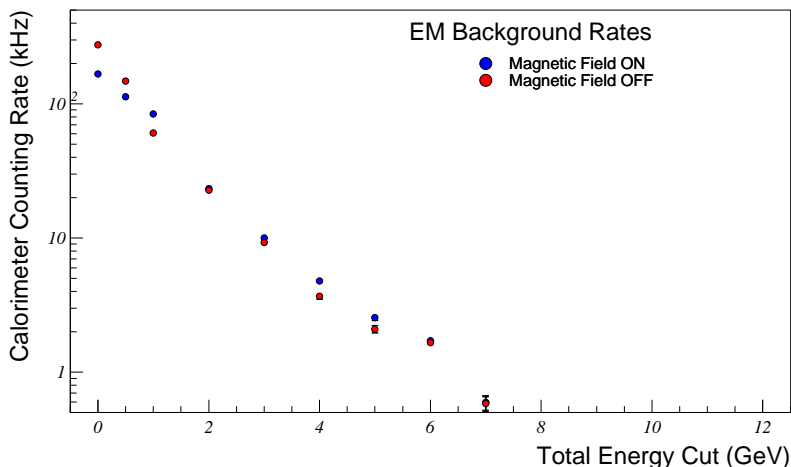


Figure 31: Counting rates of the FCAL calorimeter with the solenoid magnetic field on and off. The total energy threshold in event selection is 8.5 GeV.

8.1 Accidental Background

Photoproduction of η meson on the proton target and the electromagnetic background were simulated with the GlueX setup using standard Hall D simulation software (Geant 3 based - HDGeant). The results are shown in this section.

In order to estimate beam related backgrounds, an incoherent bremsstrahlung photon beam (see Figure 29) was incident on a 30 cm liquid hydrogen target with the solenoid magnetic field on and off. The photons pass through the entire Hall D apparatus and mainly interact with the primary collimator and the target (see Figure 30). Assuming beam intensity of $N_\gamma \sim 7.6 \times 10^6$ per second in the energy range of 10.5 GeV to 11.7 GeV on the target, simulated 8.25×10^7 events correspond to $\sim 11s$ of the beam time. For those events the counting rate of the FCAL calorimeter as a function of the total energy threshold is estimated in Figure 31 with the solenoid magnetic field on and off. As one can see, the effect of magnetic field on the counting rate of the calorimeter is small with a few GeV total energy cut. Figure 32 shows the beam related accidental background rates in the invariant mass of 2γ spectrum for different timing gates with solenoid magnetic field off. It indicates that this background in the mass of η region is small with a 4 ns timing gate.

The electromagnetic background generated from 330,000,000 photons (originated from the radiator) are shown in Figures 33 and 34. In Figure 33, the left plot shows the invariant mass and the right plot shows the total energy reconstructed from two clusters detected by the FCAL calorimeter. Figure 34 shows the occupancy of events on the calorimeter, which indicates that most of the background are concentrated near the beam line.

The time resolution of signals in the FCAL, which are recorded using Flash ADCs, is estimated to be $\sigma_t < 1$ ns [52]. We therefore believe that realistic coincidence time windows with the tagger spectrometer can be less than 4 ns. Based on these simulations, we estimate that the expected accidental rates in this experiment will be less or on the level of 0.1 Hz.

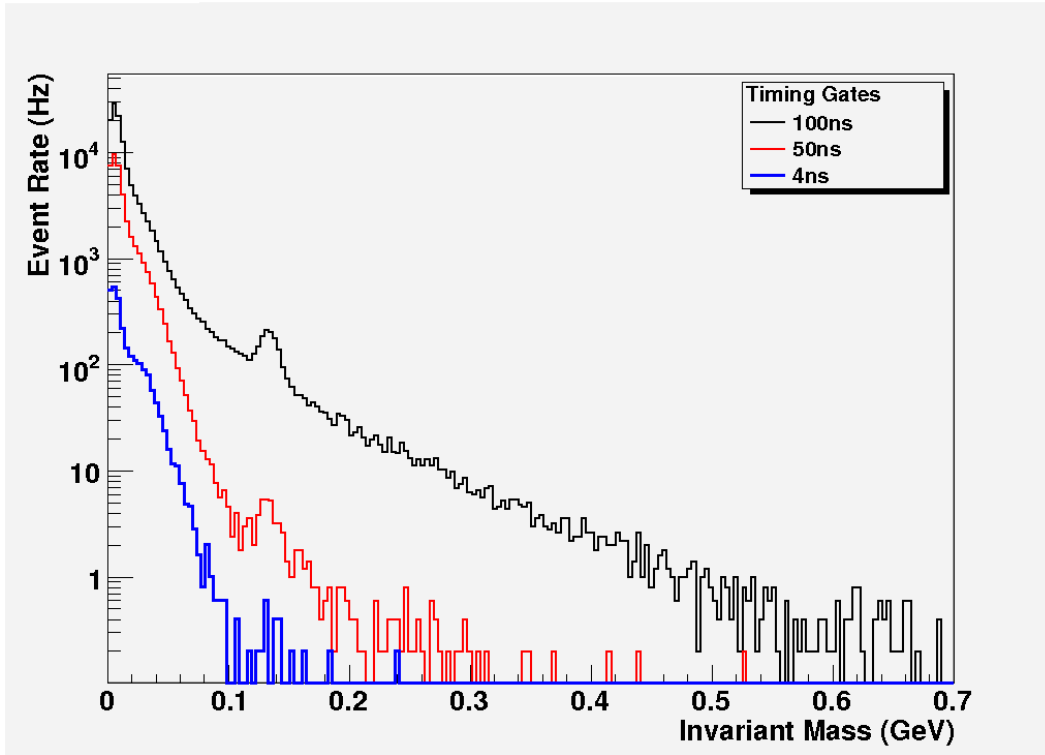


Figure 32: Accidental background rates in the 2γ invariant mass spectrum for three different timing gates. The timing gate for black curve is 100 ns, for red curve is 50 ns, and for blue curve is 4 ns.

The estimated signal rate is about 0.2 Hz (see the Section 9.1). However, the accidental events will be cut down significantly after applying the event selection cuts, and will not contribute to the background in any sizable way.

8.2 Combinatorial Background

Any two photons in the detector can contribute to accidental combinations that reconstruct to the η mass. This background can be measured accurately and subtracted, but will add to the statistical uncertainty of the signal. Therefore it is desirable to minimize such combinations. Studies show that the main contributor to combinatorial background comes from $\gamma p \rightarrow \omega p$, with $\omega \rightarrow \pi^0 \gamma$, but reconstructing only two of the three photons in the event. After standard selection cuts (see Section 7.3), the combinatorial backgrounds will be very small as shown in Table 1.

8.3 Reactions with an η in the Final State

There are several reactions with an η in the final state which can mimic the signal reaction. These include the single pion-eta reactions $\gamma p \rightarrow \eta \pi^0 p$ and $\gamma p \rightarrow \eta \pi^+ n$. Reactions with

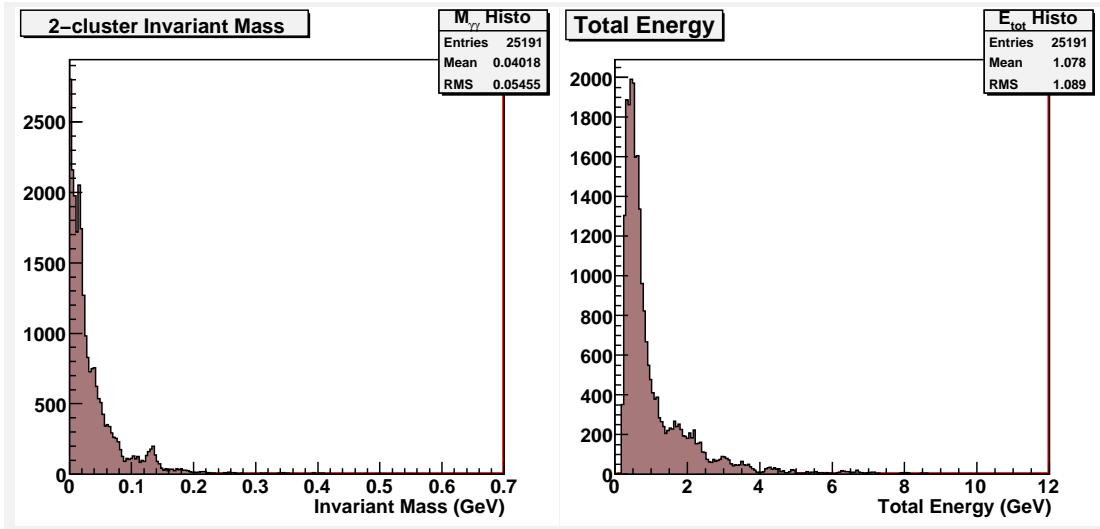


Figure 33: Distribution of invariant mass (left) and total energy (right) of the beam related background events.

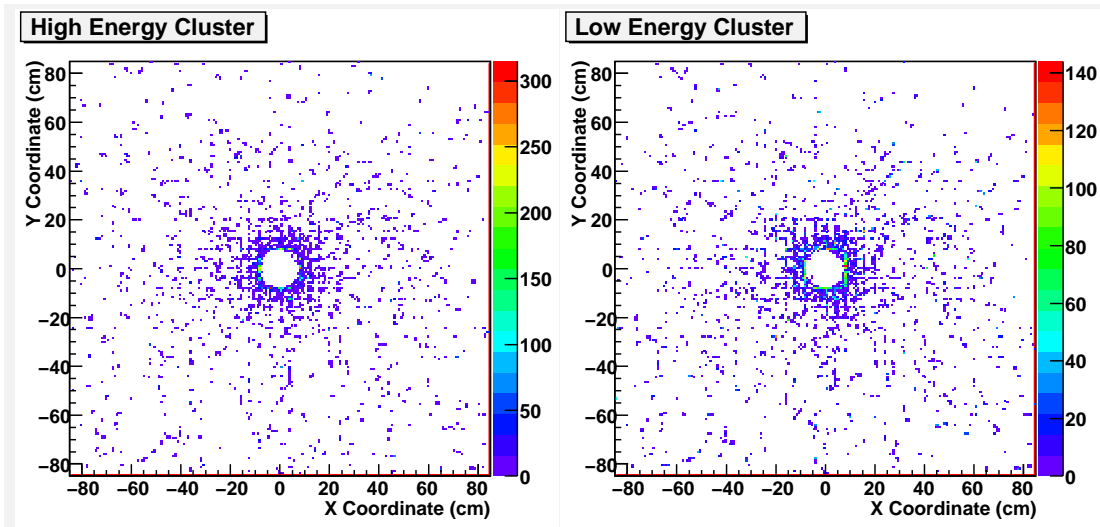


Figure 34: Cluster occupancy on the FCAL calorimeter.

Channel	Cross section (nb)	Number of events	
		$0.5 \leq \theta_\eta \leq 5.0^\circ$	$\theta_\eta \leq 0.5^\circ$
Primakov signal ($\theta_\eta \leq 0.5^\circ$)	0.64		116
Hadronic coherent	61	11138	10
$p\eta\pi^0$	190	11	1
$n\eta\pi^+$	85	55	2
$p\pi^0\gamma$	144	86	10
$p\rho^0(\eta\gamma)$		20 ± 9	0
$p\pi^0\pi^0$		4 ± 4	0
Total excluding $p\eta$		176	13 ± 4

Table 1: Estimates of signal and background rates in two angular intervals of interest. The numbers of events are normalized to a Monte Carlo sample of 80 million PYTHIA events, and with the following event selection criteria: $0.46 \text{ GeV} < m_{\gamma\gamma} < 0.62 \text{ GeV}$, $E_{bcal} < 0.06 \text{ GeV}$, and no hits in the start counter outside the angular range of $170^\circ < \phi - \phi_\eta < 190^\circ$.

multiple pions in the final state, such as $\gamma p \rightarrow \eta\pi^0\pi^0p$, can also contribute but as the number of particles in the final state increases, the likelihood that they will be confused with the kinematics and topology of $\gamma p \rightarrow \eta p$ is considerably reduced. However, at the photon energies of interest, the cross sections for multiparticle production dominate the cross section and therefore one needs to be careful that these do not feed into the sample of exclusive events.

We have used PYTHIA to generate the hadronic backgrounds for these studies. PYTHIA has been tuned at high energies and inclusive production, so the fidelity of the generated differential cross sections for exclusive reactions needs checking. In fact, the differential cross section for the signal $\gamma p \rightarrow \eta p$ is not adequately described by PYTHIA, and a special generator is used to model the signal distributions (Section 4). For single pion-eta production cross sections, we are in the process of making detailed comparisons between the PYTHIA generator and calculations by Sibirtsev [51], which are consistent with existing measure-

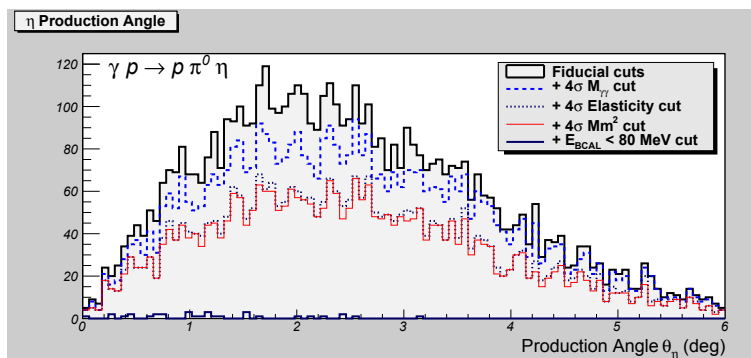


Figure 35: Distributions of θ_η for the background $\gamma p \rightarrow \eta\pi^0p$ reaction with different cuts.

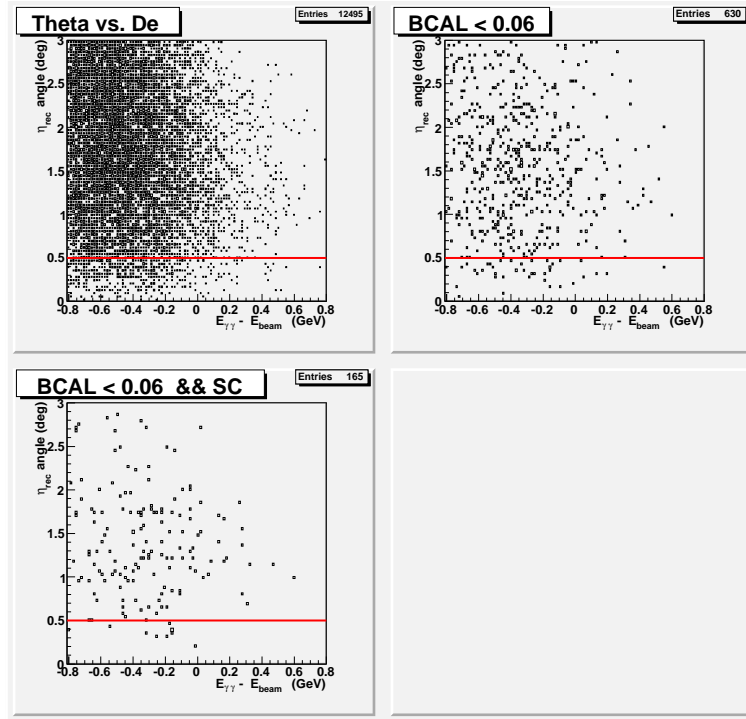


Figure 36: Distributions for the sum of the three major backgrounds $\gamma p \rightarrow \eta\pi^0 p$, $\gamma p \rightarrow \eta\pi^+ n$ and $\gamma p \rightarrow \pi^0\gamma p$. The reconstructed η scattering angle is plotted vs the difference ΔE between the two-photon and the beam energies. top left) Selection of two photon events consistent with an η , top right) Events with $E_{bcal} < 0.06$ GeV, bottom right) Events with $E_{bcal} < 0.06$ GeV and no hits in the start counter outside the angular range of $170^\circ < \phi - \phi_\eta < 190^\circ$.

ments. Preliminary comparisons show that for the $\gamma p \rightarrow \eta\pi^0 p$ reaction the agreement on the total cross section is within approximately 20%. It was noticed that PYTHIA has not accurately taking into account the helicity conservation constraint for the elastic channels, which results an enriched spectrum at forward angles for those reactions. The energy and angular distributions for reactions involving multi-pions are governed by phase-space, so we expect PYTHIA to be adequate for these reactions. For the current background studies we have used PYTHIA to model all hadronic reactions except for the signal.

These simple requirements described in the Section 7.3 eliminate essentially all hadronic backgrounds, except for $\gamma p \rightarrow \eta\pi^0 p$ and $\gamma p \rightarrow \eta\pi^+ n$. We take advantage of the benefits of the hermiticity of the Hall D detector to reject events that contain additional particles (pions) in the background reactions. The requirement that the energy in the BCAL be less than 60 MeV eliminates essentially all $\eta\pi^0 p$ events and many $\eta\pi^+ n$ events, as shown in Figure 35. However, additional cuts to eliminate events with a charged particle in the event (i.e. the π^+) are necessary to further reduce the contamination of $\eta\pi^+ n$ events. For illustration we use hit information in the start counter to achieve this goal. Fig. 36 shows the scatter plot of angle vs. missing energy for background events for these selection cuts.

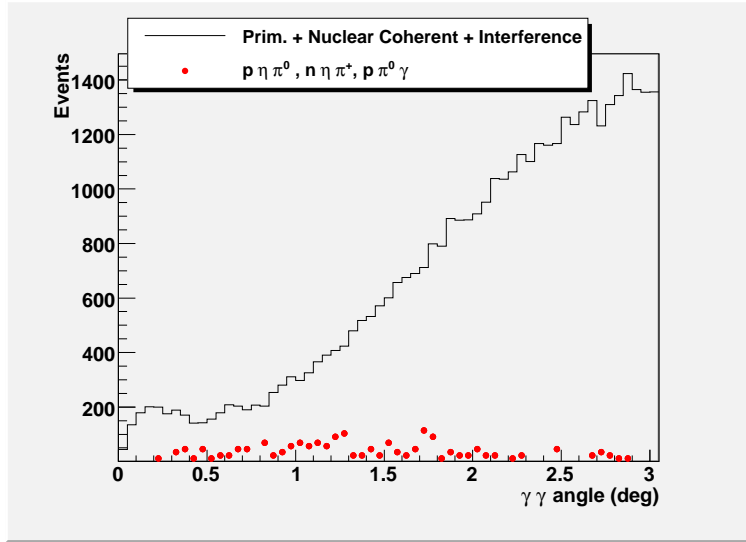


Figure 37: The θ_η angular distributions reconstructed from 2γ detected by the FCAL. The black solid curve shows the $\gamma p \rightarrow \eta p$ signal events including the Primakoff and the nuclear coherent components, and the red points are from major physics background channels discussed in the text. The event selection and BCAL energy cuts are applied. The normalization of these processes is done according to their cross sections and acceptances in the setup.

A summary of the background reduction can be found in Table 1. We see that the resulting estimated signal/background ratio below 0.5° after all cuts is about 10/1. Figure 37 is a plot of the angular distribution for signal and background following the event selection cuts to illustrate the resulting purity of the final event sample. It shows that the estimated background from the physics processes is on the level of 4% in the nuclear coherent region (about 2 degrees). The possible impact of this background on the extracted decay width is less than the systematic error shown in Table 2 and discussed in the Section 8.4. On the other hand, we note that in practice, these cuts would not be applied blindly, but rather, each background reaction would be measured over a relatively broad kinematic range outside the region of interest to determine an accurate subtraction from the signal region.

8.4 Sensitivity of $\Gamma_{\eta \rightarrow \gamma\gamma}$ Determination to Backgrounds

Like any other experiments measuring the absolute cross sections, applying the event selection cuts to select the elastic channel in the η production data set, will not completely eliminate the background contributions from other physics processes (so called the physics background). Some part of those background events will fully mimic the elastic channel. In such cases, one needs simulate the possible background contributions from identified reactions, and subtract them from the experimental yield on a bin-by-bin base. For this purpose, the cross sections of background channels should be either obtained from the theoretical cal-

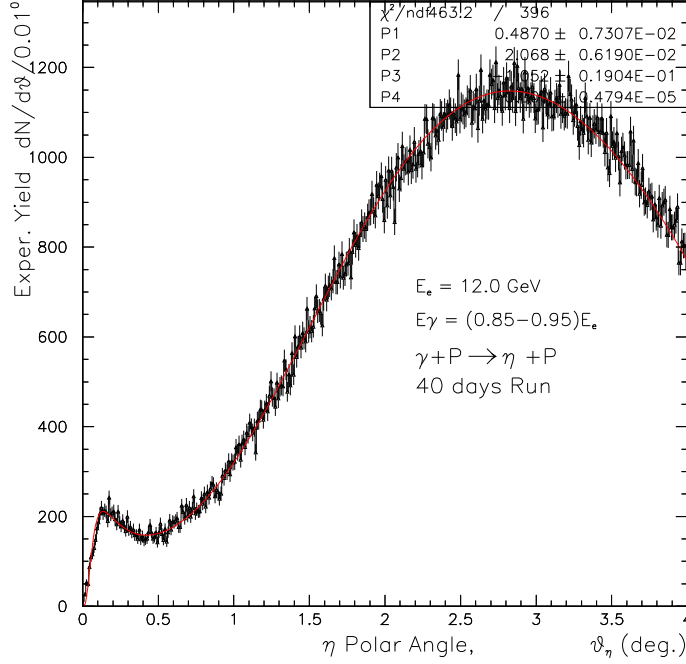


Figure 38: Monte Carlo simulation of expected yield as a function of angle for the $\gamma + p \rightarrow \eta p$ events for 40 days of running on the hydrogen target (black points). Three parameters (P1: the decay width $\Gamma_{\eta \rightarrow \gamma\gamma}$; P2: the magnitude of the nuclear coherent part; P3: the interference angle between the Primakoff and nuclear coherent processes) are kept free in the fitting procedure (solid red line).

culations or experimental measurements. In proposed experiment, the η radiative decay width will be extracted from the measured differential cross sections in the forward angles. As demonstrated in Figure 37, the contribution from the physics background is expected to be at less than 5% level. In order to study the impact on the $\Gamma_{\eta \rightarrow \gamma\gamma}$ determination due to the uncertainty of the background, we assume different levels of physics background contamination in our final angular distributions of the experimental yield. In addition, we also vary the uncertainties of the background based on the uncertainty of the cross sections known for those background reactions. Figure 39, for example, shows Monte Carlo data for 40 days of running on the proton target and a 20% level of background (the solid blue line) with a 20% uncertainty (dashed blue lines). The shape of this particular background is adjusted to the distribution obtained from the dominant $\gamma p \rightarrow \pi^0 \eta p$ background process, after the selection cuts been applied (see Figure 35). The difference between the dashed line and the solid line will be added to the distribution of Monte Carlo yield bin-by-bin to mimic the uncertainties in the background subtraction process. Then, the new distribution will be fitted to extract the $\Gamma_{\eta \rightarrow \gamma\gamma}$. As shown in Figure 40, a 20% uncertainty in the background subtraction will

result a new value for the decay width (0.494 KeV) which is different from the original non-background extraction (0.487 KeV) in Figure 38 by 1.4%. On the other hand, if we assume that the uncertainty in the background is 40%, this will result a systematic shift in the decay width about 2.8%, as shown in Figure 41. The next question is how the shape of the background distribution would affect the decay width extraction. It can be done with some assumptions also. The shape of the physics background is typically more constrained in the small forward angular region, and therefore, it has less effects on the $\Gamma_{\eta \rightarrow \gamma\gamma}$ extraction.

Based on this study and the physics background discussed in the previous Section 8, we estimate a 2% systematic error in the extracted decay width contributed from the background subtraction, which is shown in the error budget Table 2.

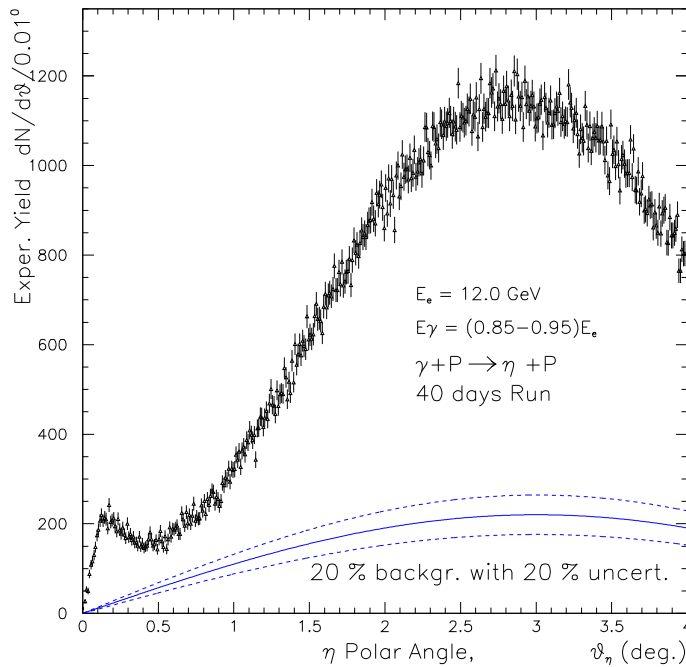


Figure 39: Angular distribution for Monte Carlo $\gamma + p \rightarrow \eta + p$ events on a hydrogen target. We assume a 20% background demonstrated by a blue solid curve, and two dashed curves show a 20% uncertainty on the background. The background level is normalized to the Monte Carlo data at 2.5 degree.

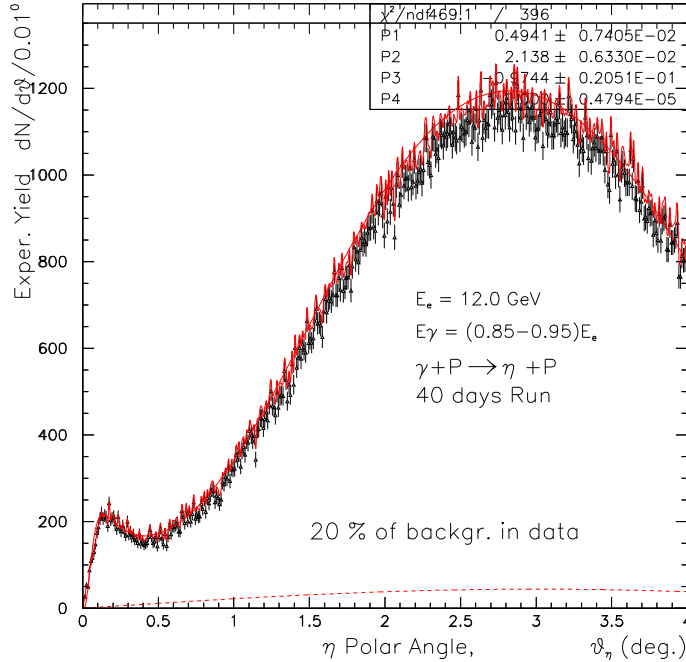


Figure 40: Angular distribution for Monte Carlo $\gamma + p \rightarrow \eta + p$ events on a hydrogen target. The black points are initial Monte Carlo signal events. The red points are signal plus additional "background" events due to a 20% uncertainty in the background subtraction. The red line shows new fitting result.

9 Rates, Uncertainties, and Beam Time Request

9.1 Production Rates

In this experiment, the Primakoff amplitude will be extracted from the measured differential cross section of the coherent η production $\gamma A \rightarrow \eta A$ (where A is p or ${}^4\text{He}$) in the forward angles. As mentioned earlier, different angular dependences for different η production mechanisms will enable separation of the Primakoff amplitude from the background nuclear coherent processes. We propose to perform a precision measurement of the differential cross sections on the proton and ${}^4\text{He}$ targets over a range of angles ($0-5^\circ$) as determined by the electromagnetic calorimeter. The FCAL calorimeter placed at a distance of ~ 5.6 m from a 30 cm long target will provide a geometrical acceptance for the two decay photons ($\eta \rightarrow \gamma\gamma$), yielding detection efficiencies of $\sim 70\%$.

In order to estimate the production rate of coherent η signal events, we assume a 7×10^7 equivalent photons/sec incoherent bremsstrahlung photon beam on target. If one takes the upper 10% energy range of the tagged photon beam from 10.5 GeV to 11.7 GeV, the number of photons is $N_\gamma \sim 7.6 \times 10^6$ photons/sec. The integral of total coherent cross sections over

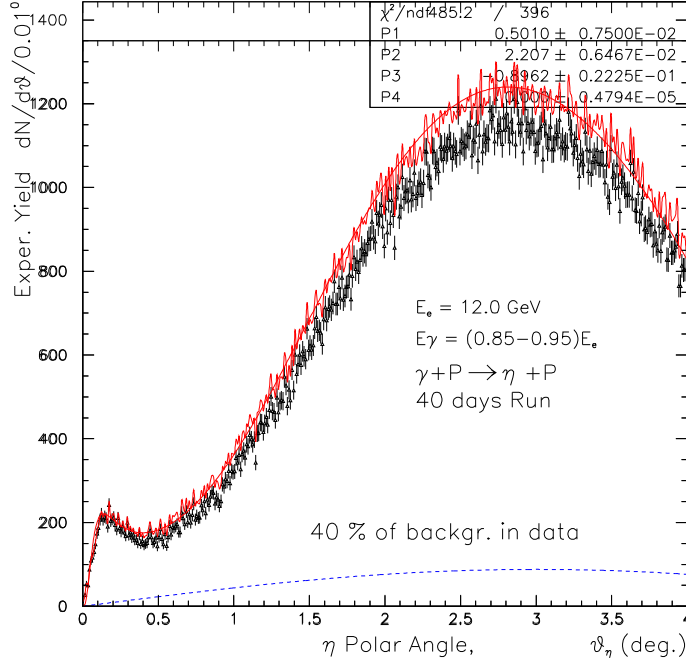


Figure 41: Angular distribution for Monte Carlo $\gamma + p \rightarrow \eta + p$ events on a hydrogen target. The black points are initial Monte Carlo signal events. The red points are signal plus additional "background" events due to a 40% uncertainty in the background subtraction. The red line shows new fitting result.

the angular range of 0-5 degrees for these energies are: ~ 61.4 nb (1.79% for Primakoff) for proton target, and ~ 16 nb (21% for Primakoff) for ${}^4\text{He}$ target.

For a 30 cm long LH_2 target (3.46% r.l., $N(p) = 1.28 \times 10^{24}$ p/cm 2), the elastic η signal event rate is estimated as follows:

$$\begin{aligned}
 N(\text{exp. ev.}) &= N(p) \times N(\gamma) \times (\text{Int. Cross Sec.}) \times (\text{eff.}) \times (\text{Br. Ratio}) \\
 &= 1.28 \times 10^{24} \times 7.6 \times 10^6 \times 61.4 \times 10^{-33} \times 0.7 \times 0.4 \\
 &\sim 0.167 \text{ (events/sec)} \\
 &\sim 14428 \text{ (total } \eta \text{ events/day)} \\
 &\sim 258 \text{ (Primakoff events/day)}
 \end{aligned}$$

The coherent η signal event rate for a 30 cm length liquid ${}^4\text{He}$ target (3.99% r.l., $N({}^4\text{He}) = 5.64 \times 10^{23}$ ${}^4\text{He}/\text{cm}^2$) is as follows:

$$\begin{aligned}
N(\text{exp. ev.}) &= N(^4\text{He}) \times N(\gamma) \times (\text{Int. Cross Sec.}) \times (\text{eff.}) \times (\text{Br. Ratio}) \\
&= 5.64 \times 10^{23} \times 7.6 \times 10^6 \times 16 \times 10^{-33} \times 0.7 \times 0.4 \\
&\sim 1.92 \times 10^{-2} \text{ (events/sec)} \\
&\sim 1659 \text{ (total } \eta \text{ events/day)} \\
&\sim 348 \text{ (Primakoff events/day)}
\end{aligned}$$

The expected experimental angular distribution from a Monte Carlo simulation on the $\gamma + p \rightarrow \eta + p$ reaction is shown in figure 38. In this simulation, the experimental resolutions and efficiencies are taken into account. The simulation corresponds to 40 days of running with a photon intensity of 7×10^7 equivalent photons/sec and a 30cm liquid hydrogen target. The simulation indicates that in 40 days of run time, more than 10,000 Primakoff events are obtained for a statistical error of better than 1%.

9.2 Uncertainties

The estimated experimental uncertainties for $\Gamma(\eta \rightarrow \gamma\gamma)$ are listed in Table 2. The first four items in the Table are estimated mostly based on our experience from the π^0 decay width experiment (PrimEx I) in Hall B [39]. In the π^0 measurement, we controlled the photon flux at 1% level by using a total absorption counter to measure the photon tagging efficiency low beam intensities and using a pair spectrometer to monitor the relative tagging efficiency at higher beam intensities. The same technique will be used in Hall D beam line. As discussed in the Section 6.1 and shown in Figure 11, if the beam centroid is aligned within 300 microns (the specification for Hall D beam line design is 200 microns), a 1% photon flux control is achievable. In addition, the quality of photon beam at the end point of the bremsstrahlung spectrum and the alignment of the experimental setup in Hall D are expected to be similar to Hall B, we estimate about 0.2% contribution from the beam energy and 0.5% from the acceptance uncertainties. In the previous π^0 measurement with ^{12}C and ^{208}Pb targets, the error from theoretical model dependence is less than 0.25%. In this proposed η experiment, using the proton target will essentially eliminate complicating factors from nuclear targets arising from nuclear incoherent process and form factor distortion in the nucleus, as discussed in the Section 5. We expect that the same level of control on model error (0.3%) or even better can be reached. Hall D is planning to use a cryogenic target system similar to what has been developed for Hall B. A 0.5% uncertainty for a 30 cm liquid target thickness is estimated using G1C and G1A CLAS results [36][37] (as discussed in the Section 6.3). The 6th item in the error budget is for $\eta \rightarrow \gamma\gamma$ branching ratio which is based on PDG value [13].

The error on event selection in most part is coming from several sources: (a) uncertainties in the efficiencies of event selection cuts; (b) the functions used to model the shapes of the signal and background; and (c) the range of spectrum used to fit the signal and background. In our previous PAC34 proposal using the HYCAL calorimeter, the total uncertainty for this item was estimated to be at 0.8% level. The FCAL resolutions are typically a factor of two less for two major selection criteria (invariant mass and elasticity). Adding them in quadrature, this gives the error on the event selection about 1.7%. As for the detection efficiency uncertainty for the experimental setup, the major contribution is coming from

photon flux	1.0%
beam energy	0.2%
acceptance, misalignment	0.5%
model dependence	0.3%
target thickness	0.5%
branching ratio	0.66% (PDG)
events selection	1.7%
detection efficiency	0.5%
background subtraction	2.0%
statistical	1.0%
Total	3.2%

Table 2: Estimation of the experimental uncertainties for $\Gamma(\eta \rightarrow \gamma\gamma)$ measurement.

the FCAL calorimeter. Based on our experience from the PrimEx experiment, the error on detection efficiency of the shower calorimeter can be controlled at 0.5% level. This was achieved by calibrating the calorimeter with a low intensity tagged photon beam to scan each calorimeter module. To the best of our knowledge, the way to calibrate FCAL calorimeter and how to determine its detection efficiency are still in the development stages. We estimate the same 0.5% error for FCAL detection efficiency and it is included in the error budget.

As discussed in the previous Section 8 and particularly in Section 8.4, the background level in this experiment is currently estimated to be at 5% level based on PYTHIA Monte Carlo simulations (see Figure 37). At this stage, considering several other factors, such as reliability of the PITHIA generator at this energy range, the estimated 5% background level might be underestimated. It can, in principle reach to 20% level. Having that in mind, we studied the impact of background subtraction on the $\Gamma_{\eta \rightarrow \gamma\gamma}$ assuming different background levels with different uncertainties (see Section 8.4). Based on this study, we estimate a 2.0% error contributed from background subtraction process.

All target sensitive systematic errors are estimated for the proton target. Based on our experience working with low Z nuclear targets, the error budget for the ^4He target in this proposal are at about the same level as the proton target which are presented in Table 2. Including a 1.0% statistical error and estimated systematic errors added in quadrature, the total error for the $\eta \rightarrow \gamma\gamma$ decay width is estimated to be on the level of 3.2% as shown in the Table 2.

9.3 Beam Time Request

In order to accumulate a data sample with statistics of 1% ($\sim 10,000$ Primakoff events) for the integrated energy interval from 10.5–11.7 GeV, we request 40 days of beam time for the LH_2 target, and 30 days for liquid ^4He target.

A summary of the requested beam time, specified for each major activity, is shown in

the table below:

LH ₂ target	40 days
⁴ He target	30 days
Empty target runs	6 days
Tagger efficiency, TAC runs	4 day
Setup, calibration, and checkout	8 days
Total	88 days

To reduce the uncertainties in the background subtraction, we plan to take empty target runs with the same conditions as the physics runs but with the liquid being emptied from the target cell. This will be done for each target. A total of 6 accumulated days will be required for these measurements. To control the photon flux in the experiment at the required 1% level, we will periodically measure the tagging efficiency with the Total Absorption Counter. This will require a minimum configuration change, and we estimate a total of 4 days for these measurements. Based on our experience from the first π^0 experiment in Hall B, we request a total of 8 days for the experimental setup calibration and complete checkout with the beam. The major part of this time will be used for the FCAL and CompCal calorimeters precision calibration, optimization, and checkout of the trigger organization for the calorimeter. The calorimeter alignment should be within a 0.7 mm accuracy in the plane perpendicular to the photon beam. Special measurements will be done for a better understanding of the FCAL and CompCal trigger efficiency.

In conclusion, we are requesting a total of 40 days of tagged photon beam time for the physics production data taking on the LH_2 target and 30 days on ^4He target. In addition, we estimate 18 days for experimental setup, calibration, and empty target runs. Therefore, we request a total of 88 days of beam time for the precision measurement of the $\eta \rightarrow \gamma\gamma$ decay width with 1% statistical error (per target) and 3% total error.

10 Verification of the Systematic Error with Compton Scattering

In this experiment, the η radiative decay width will be directly extracted from measured absolute differential cross sections of η photoproduction in forward angles. The invariant mass and the production angle of the η 's will be reconstructed by detecting the two decay photons from the $\eta \rightarrow \gamma\gamma$ reaction in the FCAL calorimeter. In order to reach the goal of the experimental accuracy, it is crucial to calibrate the overall systematic errors of the experimental setup, including the luminosity, the FCAL detection efficiency, and the experimental stability, by well known physics processes with similar kinematics in the same experimental configuration.

In our previous experiment to measure the π^0 lifetime at 6 GeV in Hall B, the HYCAL calorimeter, which was used for the π^0 detection by detecting the two photons from the $\pi^0 \rightarrow \gamma\gamma$ reaction, was also used to measure the absolute cross section of atomic electron Compton scattering on the physics target. Both scattering photon and electron were detected by the HYCAL. It provided a comprehensive check of the overall setup, as its kinematics are in many ways similar to those involved in detecting the π^0 via $\pi^0 \rightarrow \gamma\gamma$. Due to a larger central beam hole in the FCAL (a size of $12 \times 12 \text{ cm}^2$ in physical and $20 \times 20 \text{ cm}^2$ in fiducial) compared to the HYCAL (a size of $4.1 \times 4.1 \text{ cm}^2$ in physical and $8.2 \times 8.2 \text{ cm}^2$ in fiducial) and higher beam energy in the η experiment, however, there is no acceptance for the FCAL to detect both scattering photon and electron from the Compton events. We propose to add a $32.8 \times 32.8 \text{ cm}^2$ PbWO_4 crystal ($2.05 \times 2.05 \times 18 \text{ cm}^3$ per module) Compton Calorimeter (CompCal) at about 4 meters downstream of the FCAL. The CompCal has a $4.1 \times 4.1 \text{ cm}^2$ physical size central hole. For a high energy photon beam ($\sim 10.5\text{--}11.7 \text{ GeV}$), both the scattering photon and electron from the Compton events will pass through the central beam hole in the FCAL and be detected downstream by the CompCal to verify the luminosity normalization procedure (including both photon flux and target thickness). On the other hand, the Compton cross section in the lower energy range ($\sim 6.5 \text{ GeV}$) will be measured by detecting the scattering photons by the FCAL and detecting the electrons by the CompCal to monitor the systematic error of the overall experimental setup including the FCAL detection efficiency. This combination is the most feasible solution and will provide a unique opportunity to control the systematic errors of the η photoproduction cross section without changing the GlueX experimental settings.

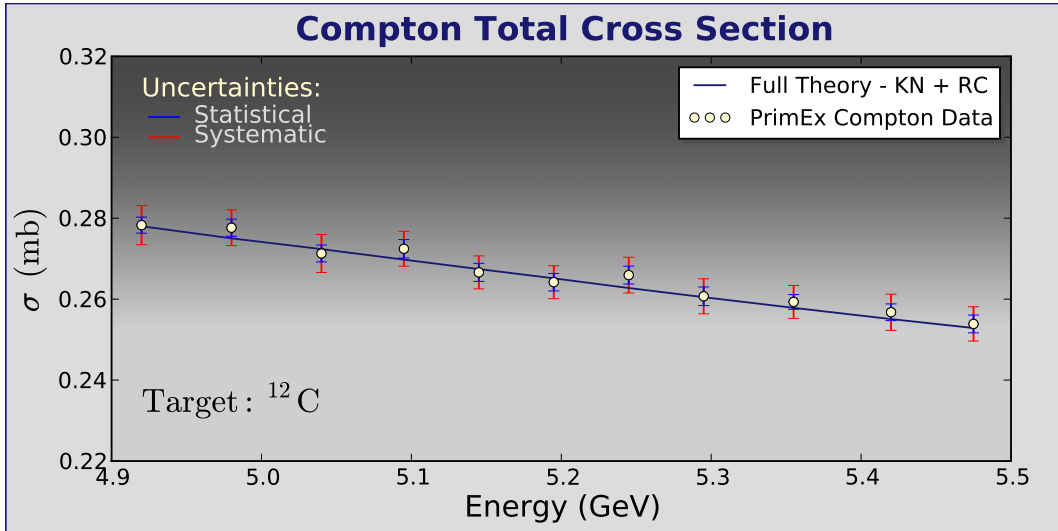


Figure 42: Measured total Compton cross section. The statistical and systematic errors are shown in blue and red respectively. The energy resolution for each point is about 1%.

The scattering of photons by free electrons $\gamma + e \rightarrow \gamma' + e'$ is one of the simplest and most basic quantum-electrodynamics processes that is experimentally accessible. The lowest order Compton scattering diagrams were first calculated by Klein and Nishina in 1929 [40],

and by Tamm in 1930 [41]. There are two types of corrections to the basic Klein-Nishina formula which must be considered when studying Compton scattering at energies above 0.1 GeV. These are radiative corrections, and double Compton scattering contributions. The interference between the basic first order single Compton scattering amplitude and the radiative and double Compton scattering amplitudes have been discussed extensively in the literature [42]-[44], [45],[46], and the errors on the theoretical calculations are less than 1%. The total Compton cross section and the forward scattering cross section with radiative and double Compton corrections have been calculated with different numerical methods[48][49]. In the case of the total cross section they are also compared to the National Institute of Standards and Technology (*NIST*) values. They are in good agreement, namely, within 0.5%. As such, Compton scattering provides an excellent means to control the systematic errors of the experiment, including the photon flux, target thickness, and the FCAL calorimeter detection efficiency.

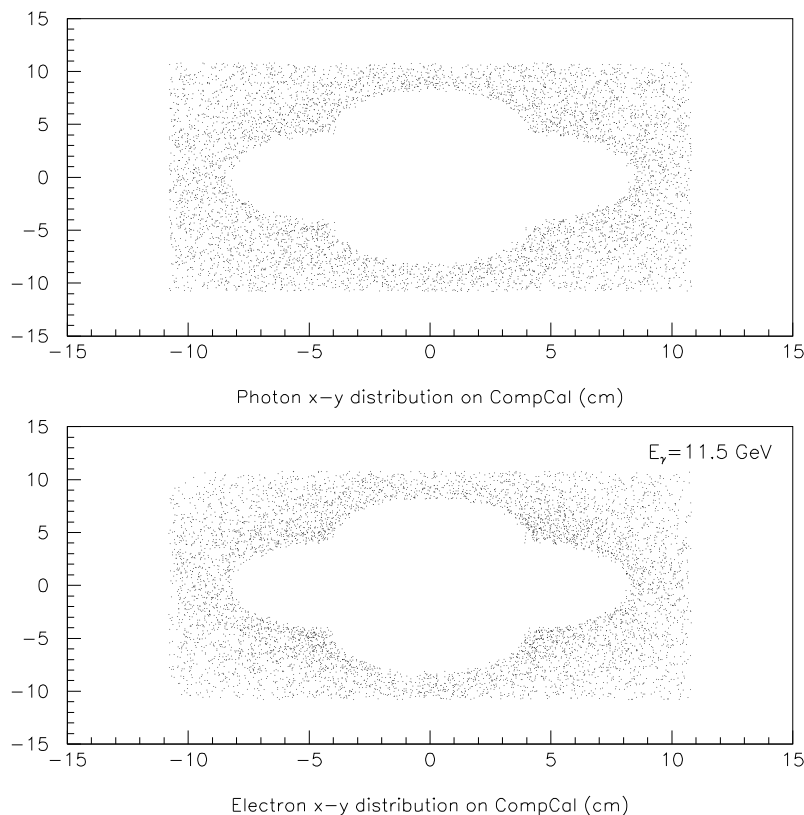


Figure 43: The x - y distributions of scattering photon-electron pairs for the Compton events at 11.5 GeV beam energy detected by the CompCal. The top plot is for photons; and the bottom plot is for electrons.

During our experiment to measure the π^0 lifetime in 2004, the Compton scattering data

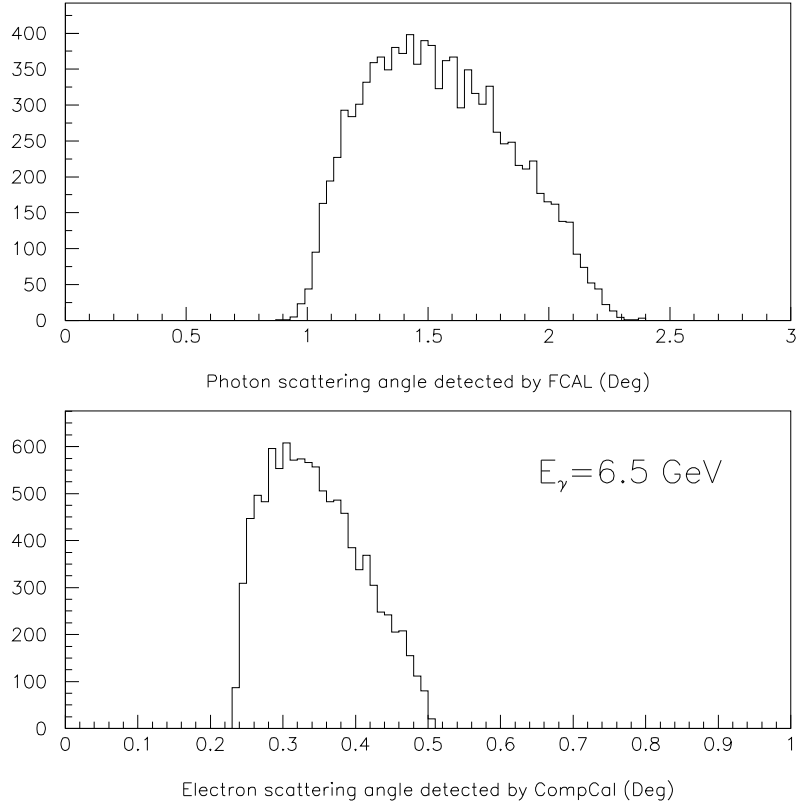


Figure 44: The scattering angular distributions of the photon-electron pairs for the Compton events at 6.5 GeV beam energy detected by FCAL (for γ) and CompCal (for e^-) in coincidence. The top plot shows the photons detected by the FCAL; and the bottom plot shows the electrons detected by the CompCal.

set was collected on a 5% radiation length ^{12}C target with incident photon beam energies of 4.85 - 5.45 GeV with a similar beam intensity as proposed η experiment. From the extracted yield, combined with luminosity and detector acceptance information, the preliminary results for the total cross section were obtained, as shown in Figures 42. These data are in excellent agreement with theory predictions with a 14% confidence level. For each data point with an energy resolution of 2% defined by two T-counters of the Hall B tagger, an average systematic error of 1.28%, a statistical error of 0.59%, and an average total error of 1.41% have been obtained. The time stability of the Compton cross section measurement was also performed and a 2% stability during the entire *PrimEx* running period (3 months) was achieved. This demonstrates that the absolute cross section measurement on Compton scattering provides an excellent tool to calibrate and monitor the *PrimEx* systematical errors.

In this proposed experiment, we plan to take Compton data in parallel with the η production runs. For higher photon beam energies, both scattered electrons and photons from

Compton scattering will be in extremely forward angles which will mostly pass through the center beam hole in the FCAL and are detected by the CompCal. The acceptance of Compton events by the CompCal will be about 5.41% for a 11.5 GeV photon beam ($\sigma_{tot} = 1.234 \times 10^{-4}$ barn), which will yield 66 Hz events rate for LH2 and 58 Hz for ^4He targets. Figure 43 shows the x and y distributions of photon-electron pairs detected by the CompCal. On the other hand, for the lower photon beam energies, the scattering photons will be in relative larger angles and detected by the FCAL; and the electrons will still mostly pass through the center beam hole in the FCAL and are detected by the CompCal. The Compton acceptance for a 6.5 GeV beam detected by both FCAL and CompCal in coincidence is about 8.5% ($\sigma_{tot} = 2.084 \times 10^{-2}$ barn), which will yield 174 Hz event rate for LH2 and 153 Hz for ^4He targets. Figure 44 shows the scattering angles of photons and electrons detected with the FCAL-CompCal combination for a 6.5 GeV photon beam. Therefore, we will open a few channels of counter in the photon tagger at about 6.5 GeV for this purpose. The combined Compton data will allow us to control the overall experimental systematic errors by measuring the absolute Compton scattering cross section at the $\sim 2\%$ level.

11 Trigger and Data Acquisition

We propose to extend the standard trigger and data acquisition (DAQ) system in Hall D to include the CompCal calorimeter. Two additional triggers will be added in order to detect Compton events: (1) a FCAL-CompCal total energy sum trigger; and (2) a CompCal total energy sum trigger. Digitization will be done using the same FADC-250 type 250MHz sampling ADC modules that will be used for the FCAL. The CompCal total energy sum will then be integrated with the FCAL energy sum to create a total energy sum for the FCAL and CompCal combined which will be used for the trigger.

Readout will use the same CODA system (with the necessary, minor configuration changes) that will be deployed for standard GlueX running. The DAQ system will be fully pipelined with no deadtime. As with GlueX, the trigger latency will be determined by the memory buffer size of the front end modules. The smallest of these being the F1-TDC-PMT module used in the photon tagger leading to a latency of $\sim 3.3\mu\text{s}$. No delay cables will be used.

12 Contribution to the Hall D Base Instrumentation

We are in the process of making strong efforts towards ensuring the overall success of the Hall D and GlueX experimental program. The specific groups and P.I.'s that will contribute to the development of the Hall D base instrumentation include: (i) North Carolina A&T State University (NCA&T), Ashot Gasparian, and (ii) University of North Carolina Wilmington (UNCW), Liping Gan. One construction MOU and one collaboration MOU between Hall D and these groups have been in process. A outline of our major responsibilities in the base instrumentation development, with institutions, is as follows:

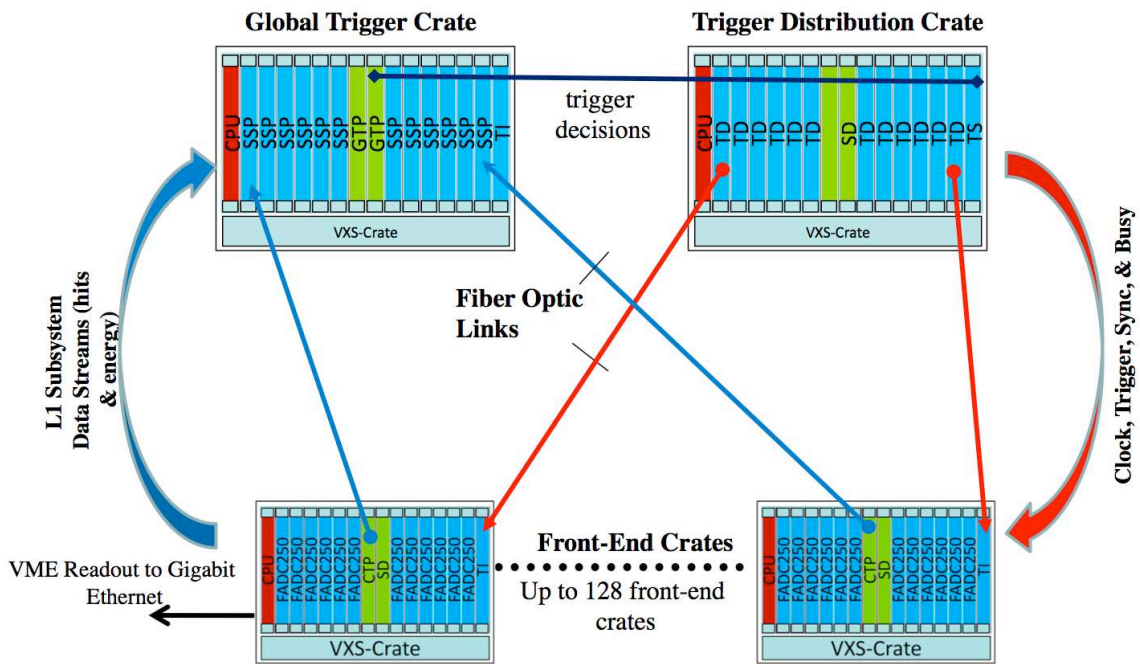


Figure 45: Schematic of the integrated triggering and DAQ system. Fiber optics continuously stream digitized energy sum information from the CTP (crate trigger processor) module in the front-end crate to the SSP (subsystem processor module) in the Global trigger crate. Trigger decisions can then be made based on total energy sums that include both the FCAL and CompCal. The addition of the CompCal will require 1 fully packed front-end crate (possibly temporarily re-tasks from the BCAL).

1. **Design and construct pair spectrometer:** UNCW group will be responsible for development of the pair Spectrometer under the construction MOU. This device is essential for 1% monitoring of the photon flux, determining the photon beam linear polarization for GlueX experiment, and providing an independent photon tagger energy calibration.
2. **Design and construct field mapper:** NCA&T group will provide scientific guidance for design and construction of magnetic field mapper. They will conduct field mapping for the pair spectrometer magnet under the collaboration MOU.
3. **Design and construct vacuum box:** NCA&T group will provide scientific guidance for design and construction of vacuum box for pair spectrometer under the collaboration MOU.
4. **Photon flux control and energy calibration:** NCA&T group will be responsible for the photon flux control and photon tagger energy calibration with the pair spectrometer under the collaboration MOU.

We also expect to contribute other areas of Hall D instrumentation, as required for the development, construction, testing and commissioning of Hall D setup.

13 Summary

We are requesting 88 days of beam time to measure the $\Gamma(\eta \rightarrow \gamma\gamma)$ decay width at a precision of 3% using the standard GlueX apparatus in Hall D. This experiment will not only resolve a long standing puzzle of the experimental discrepancy between the Primakoff and collider measurement results, but will also significantly reduce the overall error bar on this important quantity (typical errors of the existing data listed in PDG [13] are from 7.6%–25.5%), which will result a direct improvement on all other partial η decay widths as well. Precise measurement of this quantity will have a significant impact on the experimental determination of fundamental parameters of QCD, such as the ratio of light quark masses (m_u, m_d, m_s), the $\eta - \eta'$ mixing angle and their decay constants. At a more general level, this measurement will provide important test on the chiral anomaly and chiral symmetry breaking in QCD. This experiment will also deliver the first cross section measurement on the $\gamma p \rightarrow \eta p$ elementary process in 10 GeV energy range at the forward angles, which will provide important inputs in the extraction of the η photoproduction amplitude on the nucleon.

A key feature of the proposed experiment is using a tagged high energy photon beam and the choice of the light targets, particularly the proton and ^4He targets. Previous η Primakoff measurements on nuclear targets have been plagued with highly model dependent backgrounds which may very well be the source of the discrepancies between the previous collider and Primakoff results. One goal of this experiment is to address this discrepancy by measuring η photoproduction on the proton and ^4He . These two targets are complimentary. The proton will sidestep many of the complications that accompany complex nuclear targets.

On the other hand, the ${}^4\text{He}$ will have better signal to noise ratio in the Primakoff region due to its larger Primakoff cross section while it remains as the simplest compact nuclear target with the best known charge form factor.

This is the first experiment in a series of measurements planned in our Primakoff 12 GeV program. We believe the results of these future precision experiments will provide a new and powerful experimental window on QCD at JLab in an area where the basic theory has been reasonably well developed.

References

- [1] Jefferson Lab PAC18 report, 2000.
- [2] Jefferson Lab PAC23 report, 2003.
- [3] M. Gell-Mann, R. J. Oakes, and B. Renner. *Phys. Rev.* **175** (1968) 2195.
- [4] B.M.K. Nefkens and J.W. Price, *Phys. Scr.* **T99** (2002) 114.
- [5] J.S. Bell and R. Jackiw, *Nuovo Cimento* **60A** (1969) 47; S.L. Adler, *Phys. Rev.* **177** (1969) 2426.
- [6] J. L. Goity, A. M. Bernstein and B. R. Holstein, *Phys. Rev.* **D66** (2002) 076014.
- [7] B. Moussallam, *Phys. Rev.* **D51** (1995) 4939.
- [8] R. Kaiser and H. Leutwyler, *Eur. Phys. J.* **C17** (2000) 623.
- [9] Th. Feldmann and P. Kroll, *Eur. Phys. J.* **C5** (1998) 327. Th. Feldmann, P. Kroll and B. Stech, *Phys. Rev.* **D58** (1998) 114006.
- [10] P. Herrera-Siklody, J. I. Latorre, P. Pascual and J. Taron, *Nucl. Phys.* **B497** (1997) 345, and *Phys. Lett.* **B419** (1998) 326.
- [11] R. Kaiser and H. Leutwyler, in *Non-perturbative Methods in Quantum, Field Theory*, A. Schreiber, A. G. Williams and A. W. Thomas, Editors, World Scientific (Singapore 1998), hep-ph/9806336.
- [12] H. Leutwyler, *Phys. Lett.* **B374** (1996) 181.
- [13] Review of Particle Physics, *Phys. Lett.* **B667** (2008) 589.
- [14] Johan Bijnens and Jürg Gasser, Proceeding for the workshop on eta physics, Uppasala, October 25-27, 2001
- [15] A. V. Anisovich and H. Leutwyler, *Phys. Lett.* **B375**, (1996) 335.
- [16] G. Colangelo, S. Lanz and E. Passemar, arXiv:0910.0765 (2009).
- [17] D. Haidt et al (editor), *Review of Particle Physics*, Vol 3, (1998).
- [18] F. Ambrosino et al., *JHEP* **05** (2008) 006.
- [19] S. Prakhov et al., *Phys. Rev.* **C79** (2009) 035204.
- [20] C. Adolph et al., *Phys. Lett. B* **677** (2009) 24.
- [21] J. Bijnens and K. Ghorbani, *JHEP* **0711** (2007) 030.

- [22] A. Browman et al., Phys. Rev. Letts., **32**, (1974) 1067.
- [23] N.A. Roe, Phys. Rev. **D50** (1994) 1451.
- [24] A. Browman et. al., Phys. Rev. Lett. **33** (1974) 1400.
- [25] S. Gevorkyan, et al., Phys. Rev. **C80**, 055201 (2009).
- [26] S. Gevorkyan, et al., e-Print: arXiv:0908.1297[hep-ph].
- [27] T.E. Rodrigues, et. al., Phys. Rev. Lett. **101** (2008) 012301.
- [28] PrimEx collaboration, PrimEx Note 57.
- [29] G. Bellettini et al., Il Nuovo Cimento, vol. 66, no. 1, (1970), 243.
- [30] M. Guidal, J.M. Laget, and M. Vanderhaeghen, Nucl. Phys. A627, 645 (1997).
- [31] J.M. Laget, Phys Rev. **C72** (2005) 022202.
- [32] M. Branschweig, et al., DESY preprint, 70/1.
- [33] “The Technical Design of the Hall-D Polarized Photon Beam at the Thomas Jefferson National Accelerator Facility”, The GlueX Collaboration, November 7, 2008.
- [34] Jefferson Lab Hall D CDR, version 5.0.
- [35] Silvia Niccolai, *Three-body photodisintegration of ^3He measured with CLAS*, Ph.D. thesis, George Washington University, 2003, unpublished.
- [36] R. Bradford and R.A. Schumacher, CLAS-NOTE 2002-003, unpublished.
- [37] R.A. Schumacher, CLAS-NOTE 99-010, unpublished.
- [38] H. Beck et al., Nucl. Instr. Meth., **A269**, 568 (1988).
- [39] I. Larin, talk at the 2009 Jlab users’ group meeting, June 10, 2009.
http://www.jlab.org/primex/wiki/index.php/Main_Page.
- [40] O. Klein and Y. Nishina, *Z. Phys.*, **52**, 853 (1929).
- [41] I. Tamm, *Z. Phys.*, **62**, 545 (1930).
- [42] I.M. Brown and R.P. Feynman, *Phys. Rev.*, **85**, 231(1952).
- [43] Till B. Anders, *Nucl. Phys.*, **87**, 721 (1967).
- [44] K.J. Mork, *Phys. Rev.*, **A4**, 917 (1971).
- [45] F. Mandl and T.H.R. Skyrme, *Proc. R. Soc. London*, **A215**, 497 (1952).

- [46] M. Ram and P.Y. Wang, *Phys. Rev. Lett.*, **26**, 476 (1971); *ibid.* **26**, 1210(E)(1971).
- [47] A. H. Compton, Bull. Natl. Res. Counc. (U.S) 20, 19 (1922); *Phys. Rev.*, **21**, 483 (1923).
- [48] M. Konchatnyi, PrimEx Note 37.
<http://www.jlab.org/primex/>.
- [49] A. Tkabladze, M. Konchatnyi, and Y. Prok, PrimEx Note 42.
<http://www.jlab.org/primex/>.
- [50] Private communication, Richard Jones.
- [51] Private communication, Alexander Sibirtsev, Nov 2009.
- [52] J. Bennett, GlueX-doc-1258, May, 2009.